Overmodulation and six-step mode for observer-based V/Hz control

MASTER CANDIDATE

Angelica Iaderosa

Student ID 2005773

SUPERVISOR

Luigi Alberti

University of Padova

CO-SUPERVISOR

Marko Hinkkanen

Aalto University

Abstract

This thesis deals with the control of electrical machines in the overmodulation range. The goal is to have a stable control system able to exploit the full potential voltage of the inverter. After a brief explanation of the system model, the overmodulation algorithm is described. This method allows to have a smooth transition between the linear operation and the extreme operating condition in which the maximum voltage is produced. A synchronized PWM approach is adopted in order to reduce the harmonic spectrum throughout the whole operation. A scalar control based on a flux observer is considered thanks to its stability and its compatibility with the maximum voltage operation.

Results show the feasibility of the overall system, six-step mode is able to increase the reachable speed while lowering the currents.

Questa tesi tratta il controllo di macchine elettriche nel regime di sovramodulazione. L'obiettivo è ottenere un sistema di controllo stabile capace di sfruttare tutta la tensione che l'inverter è in grado di produrre. A seguito di una breve spiegazione del modello del sistema considerato, viene presentato il metodo di sovramodulazione utilizzato. Questo metodo permette di avere una transizione graduale dalla condizione lineare di funzionamento alla condizione di massima tensione ottenibile. È stata adottata una tecnica di PWM sincronizzata in modo da ridurre lo spettro armonico durante il funzionamento in regime di sovramodulazione. Il metodo di controllo utilizzato è basato su un osservatore di flusso, in questa maniera è possibile mantenere la stabilità del sistema lavorando nella condizione di massima tensione generabile.

Le simulazione confermano la fattibilità del sistema, il funzionamento in six-step permette di aumentare la velocità nella zona di indebolimento di flusso.

Contents

Symbols and abbreviations

Symbols

Operators

$\frac{\mathrm{d}}{\mathrm{d}t}$	derivative with respect to variable t
$\mathbf{I}$	identity matrix
$\mathbf{J}$	orthogonal matrix
$\mathbf{0}$	zero matrix
$T_{\alpha\beta\gamma}$	Clarke matrix
T_{dq0}	Park matrix

Model variables

B	viscous damping coefficient
$\boldsymbol{i}_{\mathrm{s}}$	stator current
$\boldsymbol{i}_{\mathrm{r}}, \boldsymbol{i}_{\mathrm{R}}, \boldsymbol{i}'_{\mathrm{R}}$	rotor current space vector in the T, Γ and inverse-Γ model
J_{m}	total moment of inertia
L_{s}	stator inductance in T model
L_{r}	rotor inductance in T model
L_{σ}, L'_{σ}	total inductance in the Γ and inverse-Γ model
$L_{\mathrm{m}}, L_{\mathrm{M}}, L'_{\mathrm{M}}$	mutual inductance in the T, Γ and inverse-Γ model
M	modulation index
m_{f}	frequency modulation ratio
R_{s}	stator resistance
$R_{\mathrm{r}}, R_{\mathrm{R}}, R'_{\mathrm{R}}$	rotor resistance in the T, Γ and inverse-Γ model
R_{σ}	total resistance in the inverse-Γ model
$u_{\mathrm{a,b,c}}$	phase voltages
$u^*_{\mathrm{a,b,c}}$	phase references
u_{dc}	DC bus voltage
$\boldsymbol{u}_{\mathrm{s}}$	stator voltage
α	inverse rotor time constant in the inverse-Γ model
δ	duty cycle
γ, γ'	scaling factor for the Γ and inverse-Γ model
$\boldsymbol{\psi}_{\mathrm{s}}$	stator flux linkage
$\boldsymbol{\psi}_{\mathrm{r}}, \boldsymbol{\psi}_{\mathrm{R}}, \boldsymbol{\psi}'_{\mathrm{R}}$	rotor flux linkage in the T, Γ and inverse-Γ model
τ_{m}	electromagnetic torque
τ_{L}	load torque
$\tau_{\mathrm{L,t}}$	speed-dependent load torque
$\tau_{\mathrm{L,w}}$	external load torque
ω_{M}	mechanical angular speed
ω_{m}	electrical angular speed

ω_{s}	stator angular frequency

Control variables

$C(s)$	compensator transfer function
$\boldsymbol{e}$	correction vector
f_{s}	sampling frequency
f_{s}	switching frequency
$F(s)$	high-pass filter transfer function
k_{ω}	positive gain
T_{s}	sampling period
T_{sw}	switching period
$\boldsymbol{u}_{\mathrm{ref}}$	reference voltage vector
$\boldsymbol{u}_{\mathrm{s,ref}}$	stator voltage reference
α_{g}	reference vector angle using Bolognani's overmodulation method
$\alpha_{1,2,\mathrm{f,o}}$	filter bandwidths
$\boldsymbol{\psi}_{\mathrm{s,ref}}$	stator flux linkage reference
$\hat{\tau}_{\mathrm{m}}$	torque estimation
$\hat{\tau}_{\mathrm{mf}}$	low-pass filtered torque stimate
$\hat{\omega}_{\mathrm{m}}$	speed estimate
$\omega_{\mathrm{s,ref}}$	external rate-limited stator frequency

Abbreviations

AC	Alternate Current
DC	Direct Current
DTC	Direct Torque Control
FOC	Field-Oriented Control
MME	Minimum Magnitude Error
MPE	Minimum Phase Error
PWM	Pulse Width Modulation
S-PWM	Sinusoidal Pulse Width Modulation
SVM	Space Vector Modulation
VSI	Voltage Source Inverter

Introduction

An electric drive is a system that converts electrical energy into mechanical energy and vice versa. Electric drives present a large variety of applications such as production plants, transportation, pumps, air compressors, but also machine tools, robotics, etc.

The main parts of an electric drive are the electrical machine and the power electronic converter together with the control system. Figure 1 shows the block scheme of an electric drive:

- the electric source can be for example a the three-phase grid or a DC source such as a battery
- the converter adjusts frequency and magnitude of voltage, it is typically made of a rectifier and an inverter;
- the motor can be for example a synchronous or an induction machine
- load and mechanical transmission form the mechanical subsystem
- the shaded region shows the control system, it comprehends the algorithms that generate all the commands to be supplied to the inverter given feedbacks provided by sensors.
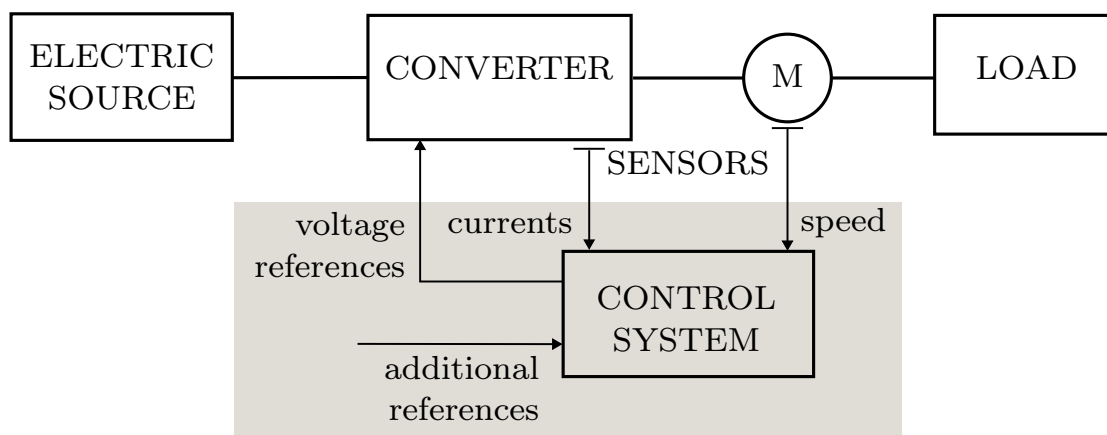

Figure 1: Block diagram of an electric drive transforming electrical energy into mechanical energy

Different types of drives differ in performance depending on the chosen control method. High performance means a wide speed range, fast and precise response in speed or position control. A first distinction among control methods can be between scalar and vector methods: scalar control is easier to implement but its dynamic is slower and less flexible; vector control, on the other hand, is more complex but more accurate. Sensorless control is possible with both types of control methods.

Scalar control is still widely used in applications such as pumps, compressors, fans, etc. where performance during transients is not a concern. It varies voltage

in relation to the supplied frequency in order to maintain the desired flux linkage. Traditional scalar control may be problematic at low speeds if no appropriate compensation is applied [1]. Many solutions were studied to avoid this issue [1–3].

Electric drives are among the best solutions for energy efficiency and decarbonisation purposes. In chemical industries, as well as in the oil and gas sector, gas engines and gas turbines were commonly used as compressors drives. Since environmental restrictions are becoming more and more stricter, the interest toward electric motors for compressors is increasing. Electrically driven centrifugal compressors are now commonly employed both in high-power and low power applications, where they can improve efficiency, decrease carbon emissions and reduce the overall size of the drivetrain although they require very high speeds [4–6].

Scalar methods, also called V/Hz control, are well-suited for high speed applications such as turbo compressors and microturbine gas generators. As a matter of fact, in most of these applications, the load does not have high starting torque or big load steps therefore no fast speed control or torque control is needed [5, 7]. The main issues related to high speed turbo compressors are high centrifugal forces, overheating and high vibrations.

Electric drives with magnetic bearings can also improve the reliability and safety of the system by eliminating the need for gearboxes and for the entire lubrication system [8].

A possible future application of high speed compressors might be hydrogen compression, in this case the challenge concerns the lighter weight of hydrogen compared to natural gas [9] that requires even higher speed.

The model considered for simulations is made of an induction motor fed by a voltage source inverter. The control method is a scalar control incorporating an observer that increases its performance [10]. Such configuration can be useful when dealing with the high speed applications described above. Despite the lower efficiency when compared to synchronous machines, induction machines are still popular because they do not require rare earth elements. Furthermore, induction machines are able to withstand high rotor temperatures and are robust when controlled by a scalar control.

The goal of this thesis is to study the compatibility between the observer-based V/Hz control and a specific operating condition called *six-step mode*. This regime occurs when the inverter is operated in such a way that the fundamental output voltage is maximized and switchings are minimized. Maximizing the voltage also means maximizing the flux linkages and, since torque is proportional to fluxes, maximizing the torque. In the flux-weakening region, having higher torque allows to increase the maximum reachable speed if assuming the typical compressor load behaviour. Six-step mode is not always feasible, control methods that include current control usually are not able to reach this operating mode. Scalar control on the other hand is able to fully utilize the inverter voltage range.

The thesis structure is the following: chapter 1 is dedicated to an overview of the system model, chapter 2 explains the theory behind the chosen control method, chapters 3 and 4 present respectively simulations and experimental results.

1. System model

This chapter presents an overview of the system model which is made of an induction machine and a voltage source inverter. In the beginning, inverter and motor model are explained using Clarke and Park transformations. Lastly the mechanical subsystem is described.

1.1 Clarke transformation

When dealing with drives, the *Clarke* transformation, also known as the $\alpha\beta$ transformation, is a useful tool.

Considering a triplet of system's electrical variables $\boldsymbol{x_{a,b,c}} = [x_a, x_b, x_c]^T$, it is possible to perform the following linear transformation

$$\begin{bmatrix} x_\alpha \\ x_\beta \\ x_\gamma \end{bmatrix} = T_{\alpha\beta\gamma} \begin{bmatrix} x_a \\ x_b \\ x_c \end{bmatrix} = \frac{2}{3} \begin{bmatrix} 1 & -1/2 & -1/2 \\ 0 & \sqrt{3}/2 & -\sqrt{3}/2 \\ 1/2 & 1/2 & 1/2 \end{bmatrix} \begin{bmatrix} x_a \\ x_b \\ x_c \end{bmatrix} \tag{1.1}$$

In geometrical terms, this transformation represents a change of coordinates, from abc to $\alpha\beta\gamma$. The new set of axes are orthogonal to one another.

When considering electrical systems with isolated neutral point, no neutral current path exist. Therefore, if the zero sequence component of a certain quantity is null, it is possible to write:

$$x_a + x_b + x_c = 0 \tag{1.2}$$

Under this particular circumstance the order of the mathematical problem is reduced by one degree since

$$x_\gamma = 0. \tag{1.3}$$

Vectors are now laying in the $\alpha\beta$ plane rather than in the tri-dimensional space. The transformation is then simplified as following:

$$\begin{bmatrix} x_\alpha \\ x_\beta \end{bmatrix} = T_{\alpha\beta} \begin{bmatrix} x_a \\ x_b \\ x_c \end{bmatrix} = \frac{2}{3} \begin{bmatrix} 1 & -1/2 & -1/2 \\ 0 & \sqrt{3}/2 & -\sqrt{3}/2 \end{bmatrix} \begin{bmatrix} x_a \\ x_b \\ x_c \end{bmatrix} \tag{1.4}$$

On the other hand, if in the system there is a non-null zero component, it is possible to isolate it and perform the transformation as follow:

$$\begin{cases} x_a = x_a{'} + x_\gamma \\ x_b = x_b{'} + x_\gamma \\ x_c = x_c{'} + x_\gamma \end{cases} \tag{1.5}$$

where the three-phase system $x_a{'}, x_b{'}, x_c{'}$ has no zero component and x_γ can be written as:

$$x_a{'} + x_b{'} + x_c{'} = 0 \qquad\qquad x_\gamma = \frac{1}{3}(x_a + x_b + x_c) \tag{1.6}$$

It can be easily shown that x_α, x_β depend only on the triplet $x_\mathrm{a}', x_\mathrm{b}', x_\mathrm{c}'$ and do not contain any zero component whatever $x_\mathrm{a}, x_\mathrm{b}$ and x_c are. This means that when operating the inverse transformation from x_α, x_β to $x_\mathrm{a}, x_\mathrm{b}, x_\mathrm{c}$, it gives the correct result only if the three phase quantities has no γ component. If not, the γ component of the transformation must be taken into account [11].

Results of the Clarke transformation in (1.4) can be written using complex notation:

$$\boldsymbol{x} = x_\alpha + \mathrm{j}x_\beta = \frac{2}{3}(x_\mathrm{a} + x_\mathrm{b}\mathrm{e}^{\mathrm{j}2\pi/3} + x_\mathrm{c}\mathrm{e}^{\mathrm{j}4\pi/3}). \tag{1.7}$$

This notation is useful to explain the inverter model.

1.2 Park transformation

Park transformation, also known as the *dq*0 transformation, is another useful tool. Starting from the three-phase system $x_\alpha, x_\beta, x_\gamma$, the system $x_\mathrm{d}, x_\mathrm{q}, x_0$ is obtained as

$$\begin{bmatrix} x_\mathrm{d} \\ x_\mathrm{q} \\ x_0 \end{bmatrix} = T_{\mathrm{dq0}} \begin{bmatrix} x_\alpha \\ x_\beta \\ x_\gamma \end{bmatrix} = \begin{bmatrix} \cos\theta & \sin\theta & 0 \\ -\sin\theta & \cos\theta & 0 \\ 0 & 0 & 1 \end{bmatrix} \begin{bmatrix} x_\alpha \\ x_\beta \\ x_\gamma \end{bmatrix} \tag{1.8}$$

where $\theta = f(t)$ is the instantaneous angle of the new coordinate system rotating with $\omega = \frac{\mathrm{d}\theta}{\mathrm{d}t}$. It is possible to make the same considerations about the zero component as for Clarke transformation. In this case the transformation reduces to

$$\begin{bmatrix} x_\mathrm{d} \\ x_\mathrm{q} \end{bmatrix} = T_{\mathrm{dq}} \begin{bmatrix} x_\alpha \\ x_\beta \end{bmatrix} = \begin{bmatrix} \cos\theta & \sin\theta \\ -\sin\theta & \cos\theta \end{bmatrix} \begin{bmatrix} x_\alpha \\ x_\beta \end{bmatrix} \tag{1.9}$$

Representation with complex notation is

$$\boldsymbol{x} = x_\mathrm{d} + \mathrm{j}x_\mathrm{q} = (x_\alpha + \mathrm{j}x_\beta)\mathrm{e}^{-\mathrm{j}\theta} = \frac{2}{3}(x_\mathrm{a} + x_\mathrm{b}\mathrm{e}^{\mathrm{j}2\pi/3} + x_\mathrm{c}\mathrm{e}^{\mathrm{j}4\pi/3})\mathrm{e}^{-\mathrm{j}\theta} \tag{1.10}$$

Figure 1.1 shows the two different set of axes. When applying to electrical machines, $\alpha\beta$ axes are referred as stator coordinates and dq axes as rotor flux coordinates.
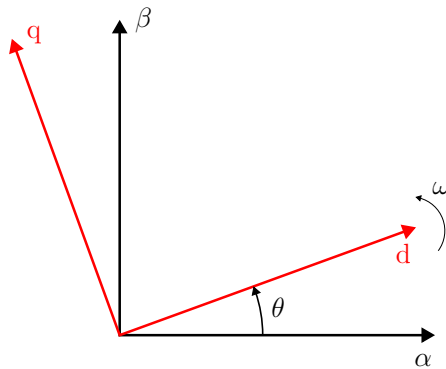

Figure 1.1: $\alpha\beta$ axes and *dq* axes

1.3 Inverter

Inverters are power electronic devices which transform DC quantities into AC quantities of desired magnitude and frequency. They are used in a large variety of electrical applications, in particular in the case of variable speed AC drives.

Figure 1.2 shows a common representation of a three phase inverter. The DC link is often modeled as a voltage source or a capacitor; the three legs are made of two switches and two antiparallel diodes, each leg supplies one of the three phases. The mid point n is almost always isolated from the ground, often it is not accessible at all.
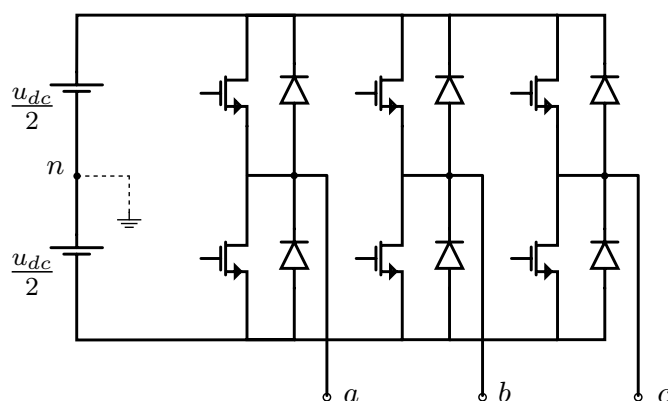

Figure 1.2: Circuit diagram of a voltage source inverter (VSI)

At any instant, each output phase voltage of the inverter can be either $u_{\mathrm{dc}}/2$ or $-u_{\mathrm{dc}}/2$, therefore there are eight possibles feasible combinations of the six switches. Using Clarke transformation in the space vector form in (1.7), it is possible to place the eight states on the $\alpha\beta$ plane obtaining the hexagon shown in figure 1.3.

The control system produces a reference of the desired output in the form of a space vector. This reference typically lays inside the hexagon so the three legs of the inverter have to be controlled together to generate it. Carrier-based approaches are the most popular choices for this purpose.
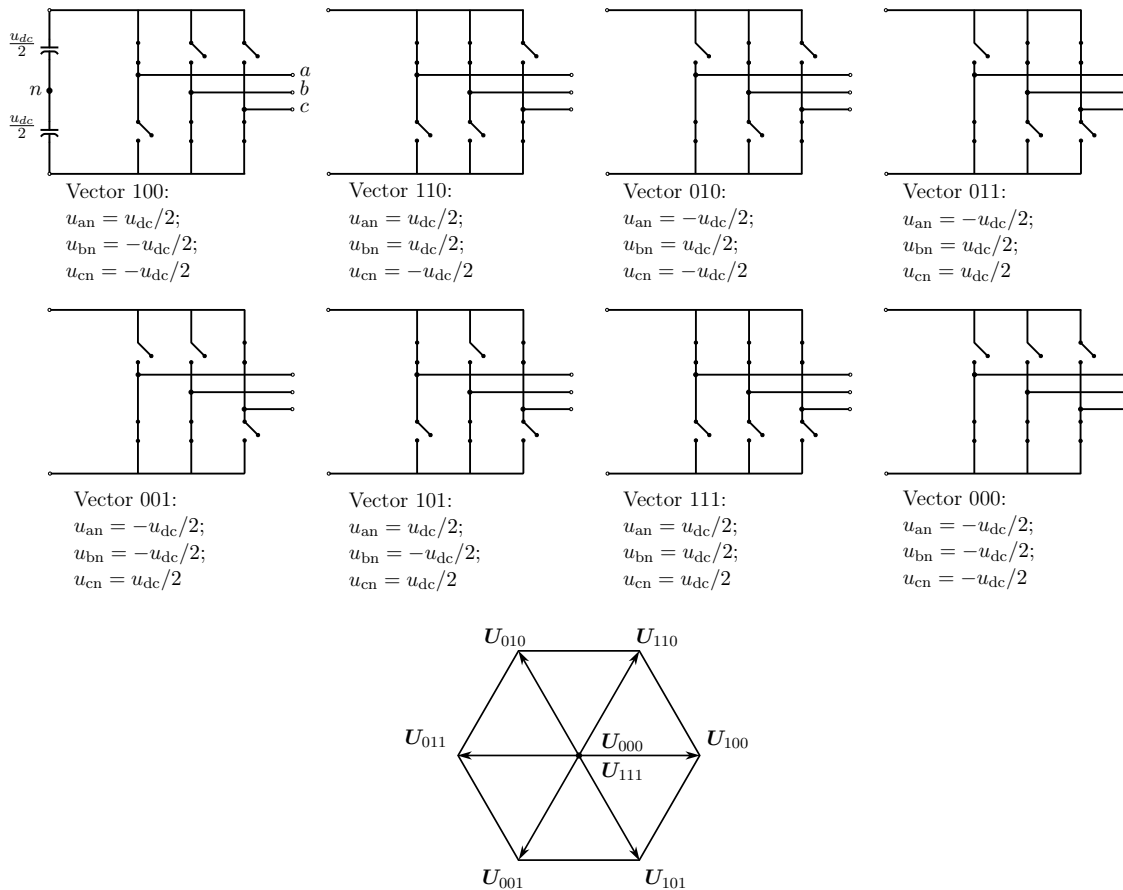
Vector 100:
$u_{an} = u_{dc}/2;$
$u_{bn} = -u_{dc}/2;$
$u_{cn} = -u_{dc}/2$

Vector 110:
$u_{an} = u_{dc}/2;$
$u_{bn} = u_{dc}/2;$
$u_{cn} = -u_{dc}/2$

Vector 010:
$u_{an} = -u_{dc}/2;$
$u_{bn} = u_{dc}/2;$
$u_{cn} = -u_{dc}/2$

Vector 011:
$u_{an} = -u_{dc}/2;$
$u_{bn} = u_{dc}/2;$
$u_{cn} = u_{dc}/2$

Vector 001:
$u_{an} = -u_{dc}/2;$
$u_{bn} = -u_{dc}/2;$
$u_{cn} = u_{dc}/2$

Vector 101:
$u_{an} = u_{dc}/2;$
$u_{bn} = -u_{dc}/2;$
$u_{cn} = u_{dc}/2$

Vector 111:
$u_{an} = u_{dc}/2;$
$u_{bn} = u_{dc}/2;$
$u_{cn} = u_{dc}/2$

Vector 000:
$u_{an} = -u_{dc}/2;$
$u_{bn} = -u_{dc}/2;$
$u_{cn} = -u_{dc}/2$

Figure 1.3: Three phase inverter output voltage vectors [11]

1.4 Carrier-based pulse width modulation

The most frequently used schemes for pulse width modulation are carrier based. These methods are characterized by subcycles T_s of constant time duration in which an active inverter leg takes on the two opposite switching states. Therefore f_{sw} is the carrier frequency with which the inverter switches are switched. Operation at f_{sw} impacts on the harmonic spectrum. It is possible to demonstrate the presence of pairs of sidebands with significant amplitudes centered around f_{sw} and its integer multiples [12, 13]. Among all the possible ways to implement carrier-based PWM, sinusoidal PWM and space vector modulation are the most popular.

When digitally implementing PWM, it is preferable to synchronize sampling and switching. Samples are taken in between switchings, coinciding with positive and negative peaks of the triangular carrier. The sampling frequency is thus selected as twice the switching frequency

$$f_s = 2f_{sw}. \tag{1.11}$$

1.4.1 Sinusoidal-PWM (S-PWM)

In a three-phase system implementing S-PWM, a common triangular carrier of frequency f_s is compared to three different reference signals called modulators. Figure

1.4 shows the three sinusoidal modulators u_a^*, u_b^*, u_c^* given by the control system and the triangular carrier u_{tr}. By comparing the carrier and the modulators, switches duty ratios, e.g. the fraction of the switching period T_{sw} in which the switch is on, are defined. u_a, u_b, u_c are the resulting phase output. Sinusoidal PWM is also known as *suboscillation method*.
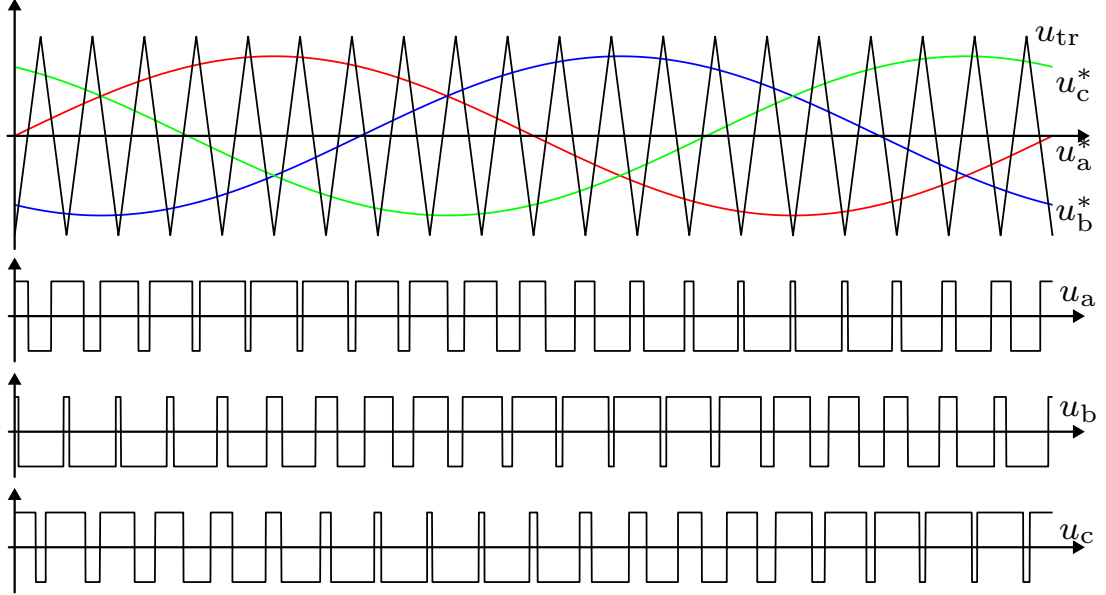

Figure 1.4: Three-pahse PWM: comparison between the three reference signals and the triangular wave [13]

1.4.2 Space vector modulation

The SVM is a carrier-based PWM method frequently used in three-phase converters with insulated neutral. It allows to maximize the voltage output while keeping linear the relation between the amplitude of the reference voltage and the output voltage. Space vector modulation differs from S-PWM in that there are not separate modulators for each phase, the reference is given as a space vector from the control system.

Given any reference vector that lays inside the hexagon, the inverter is able to realize it using the two nearest states and the zero state outputs.

As shown in figure 1.5, the reference is projected on the two nearest inverter output state vectors. Both the two states and the zero state are weighted in such a way that at the end of the modulation period the average value of the output voltage is equal to the reference given to the inverter. The length of the projections $\boldsymbol{u_1}$ and $\boldsymbol{u_2}$ determine the fraction δ of the modulation period that will be occupied by each output vector:

$$\delta_1 = \frac{|\boldsymbol{u_1}|}{|\boldsymbol{U_{100}}|} \qquad \delta_2 = \frac{|\boldsymbol{u_2}|}{|\boldsymbol{U_{110}}|} \tag{1.12}$$

The fraction occupied by the zero voltage vector can be obtained as:

$$\delta_{0,7} = 1 - \delta_1 - \delta_2 \tag{1.13}$$

The average inverter output voltage is given by:

$$\boldsymbol{u}_\mathrm{s} = \delta_1 \boldsymbol{U}_{100} + \delta_2 \boldsymbol{U}_{110} + \delta_{0,7} \boldsymbol{U}_{000,111} \tag{1.14}$$

The switching sequence and the choice between the two different zero states is made considering the minimum number of commutations possible; the transition from one state to another is performed by switching only one leg. This strategy allows to reach the minimum switching frequency of each inverter leg.
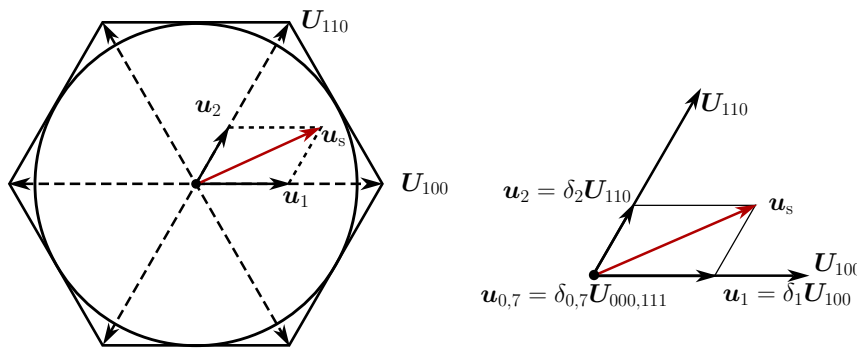

Figure 1.5: Decomposition of the reference vector in the different states [11]

The output vector and consequently duty cycles $\delta_1, \delta_2, \delta_{0,7}$ must be updated at the end of each switching period.

The inverter is usually operated with reference vectors that lay in the circle inscribed in the hexagon. Vectors laying outside the inscribed circle but still inside the hexagon are in the so-called *overmodulation region*, this condition brings distortions in the output waveforms [11]. When a vector lays partially outside the hexagon the sum of the corresponding $\delta_1, \delta_2, \delta_{0,1}$ is greater than 1 therefore the inverter is not able to generate it.

In order to further analyze this method, it is useful to define the modulation index

$$M = \frac{|\boldsymbol{u}_{\mathrm{s},1}|}{2u_\mathrm{dc}/\pi} \tag{1.15}$$

where $\boldsymbol{u}_{\mathrm{s},1}$ is the fundamental component of the phase voltage and $2u_\mathrm{dc}/\pi$ is the peak vallue of the fundamental in six-step mode [14].

Without the injection of the zero component, the maximum possible value for the modulation index is $M = 0.785$ considering as the highest voltage output in linear operation $|\boldsymbol{u}_{\mathrm{s},1}| = u_\mathrm{dc}/2$ [15]. On the other hand, when taking into account space vector modulation, the maximum value for M becomes $M = 0.907$ considering $|\boldsymbol{u}_{\mathrm{s},1}| = u_\mathrm{dc}/\sqrt{3}$ which is the radius of the inscribed circumference. Therefore, with

the injection of the zero component of the SVM technique, it is possible to generate a voltage that is almost 15% higher.

The explanation can be found looking at the reference obtained with the space vector modulation (figure 1.6): the output phase voltage obtained by the SVM method is not sinusoidal, it contains harmonics of triplen order. These harmonics do not pose any problem because they disappear while considering the output phase-to-phase voltage.
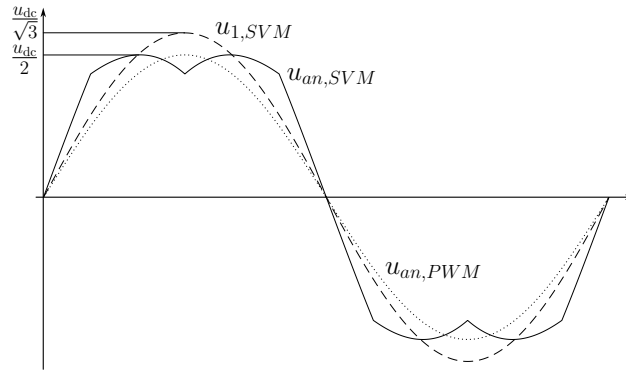

Figure 1.6: SVM inverter reference waveform; comparison between the fundamental components obtained by PWM without zero component (dotted line) and SVM (dashed line) [15]

As a matter of fact, when looking deeper at the eight possible states in figure 1.3 it is possible to notice that they do not comply with the condition in (1.2) because the γ component is not zero.

$$\begin{bmatrix} u_{100,\alpha} \\ u_{100,\beta} \\ u_{100,\gamma} \end{bmatrix} = T_{\alpha\beta\gamma} \begin{bmatrix} \frac{1}{2}u_{dc} \\ -\frac{1}{2}u_{dc} \\ -\frac{1}{2}u_{dc} \end{bmatrix} = \frac{2}{3} \begin{bmatrix} 1 & -1/2 & -1/2 \\ 0 & \sqrt{3}/2 & -\sqrt{3}/2 \\ 1/2 & 1/2 & 1/2 \end{bmatrix} \begin{bmatrix} \frac{1}{2}u_{dc} \\ -\frac{1}{2}u_{dc} \\ -\frac{1}{2}u_{dc} \end{bmatrix} = \begin{bmatrix} \frac{2}{3}u_{dc} \\ 0 \\ -\frac{1}{6}u_{dc} \end{bmatrix} \tag{1.16}$$

Therefore a better representation of the inverter output vectors could be the one shown in figure 1.7 keeping in mind that the $\alpha\beta\gamma$ axes are orthogonal to one another.
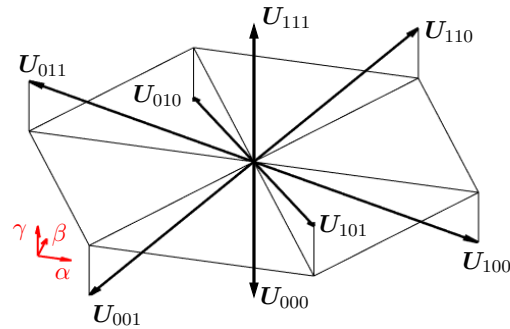
Figure 1.7: Three dimensional view of the space vector hexagon [11]

1.5 Induction motors

Induction machines were invented by Nikola Tesla in 1887. Despite the introduction of more advanced machines, induction machines still hold the largest share of the market. The main reasons for their success are the low manufacturing cost, the mechanical robustness and the high reliability.

Induction machines are made of two parts: rotor and stator. The stator is made of a laminated iron core with slots in which a three-phase winding is placed. The rotor circuit is typically made by aluminum bars (squirrel cage rotor) die-casted in a solid core made with laminated iron. When the stator winding is fed with current, it generates a rotating magnetic field that induces current in the rotor bars. In accordance with Lenz's law, the rotor starts to rotate in the direction of the rotating magnetic field in order to oppose to the variation in current.

The stator current is represented by a real column vector $\boldsymbol{i}_s = [i_{sd}, i_{sq}]^T$ whose elements are defined by Park transformation in (1.9), the superscript T mark the transpose. Other vector quantities are represented similarly. Furthermore, the identity matrix $\mathbf{I} = \left[\begin{smallmatrix} 1 & 0 \\ 0 & 1 \end{smallmatrix}\right]$, the orthogonal matrix $\mathbf{J} = \left[\begin{smallmatrix} 0 & -1 \\ 1 & 0 \end{smallmatrix}\right]$ and the zero matrix $\mathbf{0} = \left[\begin{smallmatrix} 0 & 0 \\ 0 & 0 \end{smallmatrix}\right]$ are used in the following equations.

1.5.1 Induction motor models

Figure 1.8 shows the so-called *T model* of an induction motor. In this scheme the flux linkages are formulated as

$$\begin{bmatrix} \boldsymbol{\psi}_s \\ \boldsymbol{\psi}_r \end{bmatrix} = \begin{bmatrix} L_s & L_m \\ L_m & L_r \end{bmatrix} \begin{bmatrix} \boldsymbol{i}_s \\ \boldsymbol{i}_r \end{bmatrix} \tag{1.17}$$

where L_s and L_r stand respectively for stator and rotor inductance while L_m represents the mutual inductance between the two.

12

Stator and rotor voltage equations can be respectively expressed as

$$\boldsymbol{u}_{\mathrm{s}} = R_{\mathrm{s}}\boldsymbol{i}_{\mathrm{s}} + \frac{\mathrm{d}\boldsymbol{\psi}_{\mathrm{s}}}{\mathrm{d}t} \tag{1.18a}$$

$$\boldsymbol{0} = R_{\mathrm{r}}\boldsymbol{i}_{\mathrm{r}} + \frac{\mathrm{d}\boldsymbol{\psi}_{\mathrm{r}}}{\mathrm{d}t} + \omega_{\mathrm{m}}\mathbf{J}\boldsymbol{\psi}_{\mathrm{r}} \tag{1.18b}$$

where R_{s} and R_{r} are respectively stator and rotor resistance and ω_{m} is the electrical speed of the motor. Rotor voltage is assumed equal to zero because of the shortcircuit rings.
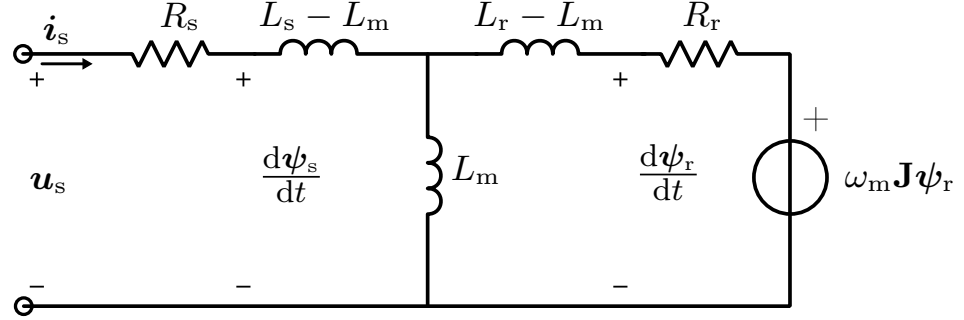

Figure 1.8: T model of induction machine

The *T model* has a practical limit: rotor parameters are not accessible for measurement. It can be simplified without loss of accuracy into the Γ *model* shown in figure 1.9. The parameters and the system equations are derived by using the scaling factor

$$\gamma = \frac{L_{\mathrm{r}}}{L_{\mathrm{m}}} \tag{1.19}$$

Therefore the rotor variables become

$$\boldsymbol{i}_{\mathrm{R}} = \frac{\boldsymbol{i}_{\mathrm{r}}}{\gamma}$$
$$\boldsymbol{\psi}_{\mathrm{R}} = \gamma\boldsymbol{\psi}_{\mathrm{r}} \tag{1.20}$$

Flux linkages can now be expressed as

$$\boldsymbol{\psi}_{\mathrm{s}} = L_{\mathrm{m}}(\boldsymbol{i}_{\mathrm{s}} + \boldsymbol{i}_{\mathrm{R}})$$
$$\boldsymbol{\psi}_{\mathrm{R}} = L_{\mathrm{m}}(\boldsymbol{i}_{\mathrm{s}} + \boldsymbol{i}_{\mathrm{R}}) + L_{\sigma}\boldsymbol{i}_{\mathrm{R}} \tag{1.21}$$

and voltage equations become

$$\boldsymbol{u}_{\mathrm{s}} = R_{\mathrm{s}}\boldsymbol{i}_{\mathrm{s}} + \frac{\mathrm{d}\boldsymbol{\psi}_{\mathrm{s}}}{\mathrm{d}t} \tag{1.22a}$$

$$0 = R_{\mathrm{R}}\boldsymbol{i}_{\mathrm{R}} + \frac{\mathrm{d}\boldsymbol{\psi}_{\mathrm{R}}}{\mathrm{d}t} + \omega_{\mathrm{m}}\mathbf{J}\boldsymbol{\psi}_{\mathrm{R}} \tag{1.22b}$$

With the scaled parameters

$$L_{\mathrm{M}} = \gamma L_{\mathrm{m}} = L_{\mathrm{s}}$$
$$L_{\sigma} = \gamma(L_{\mathrm{s}} - L_{\mathrm{m}}) + \gamma^2(L_{\mathrm{r}} - L_{\mathrm{s}})$$
$$R_{\mathrm{R}} = \gamma^2 R_{\mathrm{r}} \tag{1.23}$$

Figure 1.9: Γ model of induction machine

In order to derive the *inverse-Γ model* in figure 1.10, the scaling factor γ' needs to be defined as

$$\gamma' = \frac{L_{\mathrm{m}}}{L_{\mathrm{r}}} \tag{1.24}$$

In this case flux linkages and voltage equations become

$$\begin{aligned}
\boldsymbol{\psi}_{\mathrm{s}} &= L'_\sigma \boldsymbol{i}_{\mathrm{s}} + L'_{\mathrm{M}}(\boldsymbol{i}_{\mathrm{s}} + \boldsymbol{i}'_{\mathrm{R}}) \\
\boldsymbol{\psi}'_{\mathrm{R}} &= L'_{\mathrm{M}}(\boldsymbol{i}_{\mathrm{s}} + \boldsymbol{i}'_{\mathrm{R}})
\end{aligned} \tag{1.25a}$$

$$\begin{aligned}
\boldsymbol{u}_{\mathrm{s}} &= R_{\mathrm{s}}\boldsymbol{i}_{\mathrm{s}} + \frac{\mathrm{d}\boldsymbol{\psi}_{\mathrm{s}}}{\mathrm{d}t} \\
0 &= R'_{\mathrm{R}}\boldsymbol{i}'_{\mathrm{R}} + \frac{\mathrm{d}\boldsymbol{\psi}'_{\mathrm{R}}}{\mathrm{d}t} + \omega_{\mathrm{m}}\mathbf{J}\boldsymbol{\psi}'_{\mathrm{R}}
\end{aligned} \tag{1.25b}$$

With the scaled parameters

$$\begin{aligned}
L'_{\mathrm{M}} &= \gamma' L_{\mathrm{m}} \\
L'_\sigma &= (L_{\mathrm{s}} - L_{\mathrm{m}}) + \gamma'(L_{\mathrm{r}} - L_{\mathrm{s}}) \\
R'_{\mathrm{R}} &= \gamma'^2 R_{\mathrm{r}}
\end{aligned} \tag{1.26}$$

In all the models the electromagnetic torque can be computed as

$$\tau_{\mathrm{m}} = \frac{3}{2}p\boldsymbol{i}_{\mathrm{s}}^{\mathrm{T}}\mathbf{J}\boldsymbol{\psi}_{\mathrm{s}}. \tag{1.27}$$
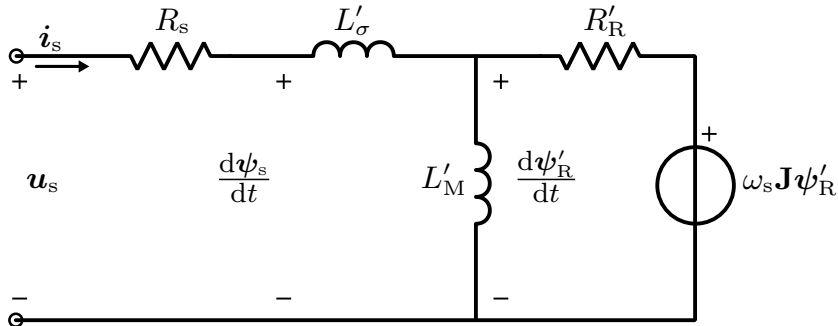
Figure 1.10: Inverse-Γ model of induction machine

Both the *Γ model* and the *inverse-Γ model* are well suited for the control of electric drives [16].

Stator current $\boldsymbol{i}_\text{s}$ and rotor flux linkage $\boldsymbol{\psi}'_\text{R}$ are the state variables, the corresponding non-linear state equations can be found combining (1.25a) and (1.25b) and then transforming into rotor flux coordinates using (1.9):

$$L'_\sigma \frac{\mathrm{d}\boldsymbol{i}_\text{s}}{\mathrm{d}t} = - (R_\sigma \mathbf{I} + \omega_\text{s} L'_\sigma \mathbf{J})\boldsymbol{i}_\text{s} + (\alpha \mathbf{I} - \omega_\text{m}\mathbf{J})\boldsymbol{\psi}'_\text{R} + \boldsymbol{u}_\text{s} \tag{1.28a}$$

$$\frac{\mathrm{d}\boldsymbol{\psi}'_\text{R}}{\mathrm{d}t} = R'_\text{R}\boldsymbol{i}_\text{s} - (\alpha \mathbf{I} + \omega_\text{r}\mathbf{J})\boldsymbol{\psi}'_\text{R} \tag{1.28b}$$

where $R_\sigma = R_\text{s} + R'_\text{R}$ is the total resistance, $\alpha = R'_\text{R}/L'_\text{M}$ is the inverse rotor time constant and $\omega_\text{r} = \omega_\text{s} - \omega_\text{m}$ is the slip angular frequency.

Figure 1.11 shows the block scheme of the motor model. The *magnetic model* block includes flux and torque equations respectively in (1.25a) and (1.27). Optionally, it can include saturation characteristics.
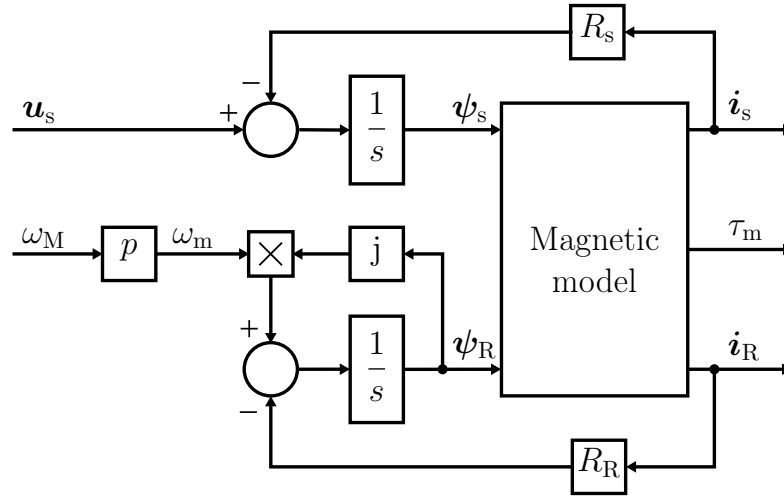

Figure 1.11: Block diagram of the motor model

1.5.2 Mechanical subsystem

The coupling between motor and load is modeled as rigid so it can be described as:

$$J_\text{m}\frac{\mathrm{d}\omega_\text{M}}{\mathrm{d}t} = \tau_\text{m} - \tau_\text{L} \tag{1.29}$$

where J_m is the total moment of inertia of motor and load reduced to motor shaft and τ_L is the load torque.

The total load torque is

$$\tau_\text{L} = \tau_\text{L,w} + \tau_\text{L,t} \tag{1.30}$$

where $\tau_\text{L,w}$ is the speed-dependent load torque and $\tau_\text{L,t}$ is the external load torque as a function of time. The second term depends on the type of load connected to the system. A typical speed-dependent load component is viscous friction

$$\tau_\text{L,w} = B\omega_\text{M} \tag{1.31}$$

where B is the viscous damping coefficient. Another typical speed-dependent load torque profile is quadratic load torque:

$$\tau_{\mathrm{L,w}} = k\omega_{\mathrm{M}}^2 \mathrm{sign}(\omega_{\mathrm{M}}) \tag{1.32}$$

which is common for pumps, compressors and fans as well as for vehicles moving at higher speeds due to air resistance [17].

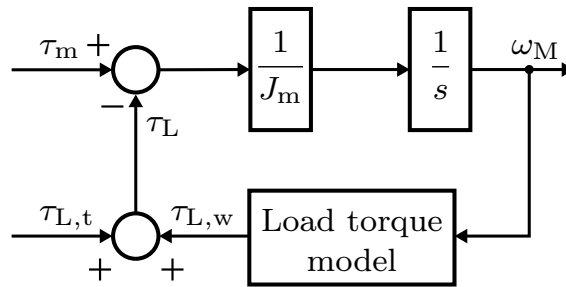Figure 1.12: Block diagram of the stiff mechanics

2. Methods

This chapter presents the technique used to operate the voltage source inverter and the control scheme chosen for the system. Sections 2.1 and 2.2 present the SVM implementation and the overmodulation management. Section 2.3 explains the principle of synchronized PWM and, lastly, section 2.4 presents the most common control methods with a focus on the observer-based V/Hz control used for simulations.

2.1 The magnitude rule

The procedure for implementing the SVM described in the previous chapter requires multiple steps in each modulation period it. Given the α and β component of the reference voltage, the steps are:

- locate the sector where the reference vector is laying
- calculate the length of the projections of the reference vector U_1, U_2
- compute the duty cycles $\delta_1, \delta_2, \delta_{0,7}$
- compute the duty cycles $\delta_a, \delta_b, \delta_c$ of the three legs of the inverter

There is an easier way to implement the SVM technique. It requires to look at PWM and SVM from another perspective [18]. It has been already discussed the importance of injecting a zero component in the voltage in order to achieve the maximum output available. It is possible to give an alternative explanation to better understand the concept.

Starting from the sinusoidal PWM explained in section 1.4.1, the first step is to make the switching instants symmetrical within the switching period T_{sw} as shown in figure 2.1a. Since the phase voltages are referred to the neutral point, the voltage can be computed in the following way:

$$u_{\mathrm{a,b,c}} = \frac{1}{T_{\mathrm{sw}}} \left[t_+^{\mathrm{a,b,c}} \frac{u_{\mathrm{dc}}}{2} + t_-^{\mathrm{a,b,c}} \frac{u_{\mathrm{dc}}}{2} \right] = \frac{s_{\mathrm{a,b,c}} u_{\mathrm{dc}}}{2} \tag{2.1}$$

where T_{sw} is the switching period, $t_+^{\mathrm{a,b,c}}$ and $t_-^{\mathrm{a,b,c}}$ are respectively the intervals in which the upper and the lower switches of figure 1.3 are conducting. $s_{\mathrm{a}}, s_{\mathrm{b}}, s_{\mathrm{c}}$ are the reference signal amplitudes $u_{\mathrm{a}}, u_{\mathrm{b}}, u_{\mathrm{c}}$ scaled by $u_{\mathrm{dc}}/2$. These signals are ranging between 0 and 1.

Using the simplified Clarke transformation in (1.4) we can transform the triplet of phase voltages $u_{\mathrm{a}}, u_{\mathrm{b}}, u_{\mathrm{c}}$ in u_{α}, u_{β} with:

$$\begin{bmatrix} u_{\alpha} \\ u_{\beta} \end{bmatrix} = \frac{2}{3} \begin{bmatrix} 1 & -1/2 & -1/2 \\ 0 & \sqrt{3}/2 & -\sqrt{3}/2 \end{bmatrix} \begin{bmatrix} u_{\mathrm{a}} \\ u_{\mathrm{b}} \\ u_{\mathrm{c}} \end{bmatrix} = \frac{u_{\mathrm{dc}}}{2} \begin{bmatrix} 2/3 & -1/3 & -1/3 \\ 0 & 1/\sqrt{3} & -1/\sqrt{3} \end{bmatrix} \begin{bmatrix} s_{\mathrm{a}} \\ s_{\mathrm{b}} \\ s_{\mathrm{c}} \end{bmatrix} \tag{2.2}$$

It is possible to observe that if the same quantity Δ is subtracted from all the reference signals $s_{\mathrm{a,b,c}}' = s_{\mathrm{a,b,c}} - \Delta$, a zero component is added. The resulting space

(a) Suboscillation method

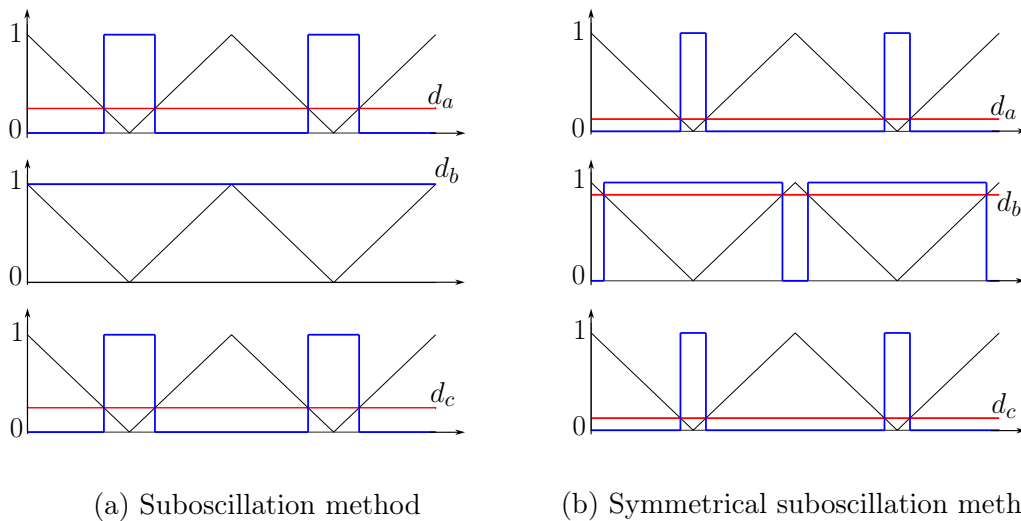(b) Symmetrical suboscillation method

Figure 2.1: Suboscillation and symmetrical suboscillation methods: $u_{\text{a,ref}} = u_{\text{c,ref}} = -u_{\text{dc}}/4$ and $u_{\text{b,ref}} = u_{\text{dc}}/2$

vector is not altered as explained in the previous chapter. In order to operate in the hexagon it is necessary to choose Δ in order to achieve:

$$\max(s_{\text{a}}', s_{\text{b}}', s_{\text{c}}') = -\min(s_{\text{a}}', s_{\text{b}}', s_{\text{c}}') \tag{2.3}$$

The value of Δ comes as:

$$\Delta = \frac{\max(s_{\text{a}}', s_{\text{b}}', s_{\text{c}}') + \min(s_{\text{a}}', s_{\text{b}}', s_{\text{c}}')}{2} \tag{2.4}$$

The space vector modulation implies that the reference signal is symmetrical with respect to the maximum and the minimum value, as shown in figure 2.1b, hence the other name *Symmetrical Suboscillation Method*.

The procedure in (2.4) requires a small number of computations and therefore can be easily implemented [18].

2.2 Overmodulation region

As discussed before, the relation between the reference vector and the SVM output is linear until the amplitude reaches the inscribed circumference, $|\boldsymbol{u}_{\text{ref}}| = u_{\text{dc}}/\sqrt{3}$. However the inverter is able to generate every reference vector that lays in the hexagon. When the amplitude ranges between $|\boldsymbol{u}_{\text{ref}}| = u_{\text{dc}}/\sqrt{3}$ and $|\boldsymbol{u}_{\text{ref}}| = 2u_{\text{dc}}/3$ the vector lays in the so-called overmodulation region.

In the overmodulation region the drive performance degrades [14] but operating in this region is still needed sometimes. When using vector control, the overmodulation region is usually reached during transients. Figure 2.2 shows two of the most used ways to manage overmodulation with vector control: Minimum Phase Error (MPE) and Minimum Magnitude Error (MME), respectively blue and red points. According to MPE, the vector is produced by keeping the same angle as

the original reference and limiting its magnitude to the hexagon boundary. On the other hand, with MME method, the vector is found projecting the reference on the hexagon boundary [19, 20]. These two methods allow to synthesize references that lay outside the hexagon but they do not exploit the full inverter voltage.

On the other hand, V/Hz control can operate in the overmodulation region during steady-state operation using the so-called *six-step mode*. Bolognani's method in [21] allows to reach six-step with a simple algorithm.
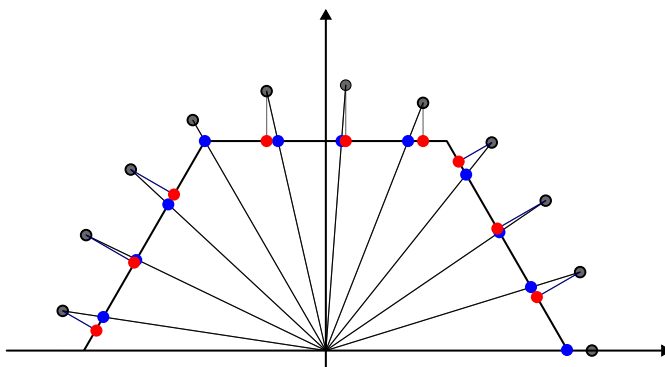
Figure 2.2: Vector-space illustration of common overmodulation methods: MPE in blue, MME in red

2.2.1   Six-step mode

Six-step mode is an overmodulation technique that consists of using only the six state vectors in figure 1.3. As shown in figure 2.3a, the reference vector is approximated as the nearest output state voltage and kept the same for all the modulation period. Figure 2.3b shows the comparison between SVM output and six-step mode. When operating in six-step mode the output reference phase voltage is a square-wave, in this way it is possible to fully utilize the inverter output voltage and maximize the torque production in the field-weakening region. Furthermore, the inverter switching frequency is reduced to six times fundamental frequency which significantly reduces switching losses. On the other hand, the harmonic spectrum is larger and losses in the motor tend to increase.

Six-step is convenient when dealing with applications such as compressors that do not require high dynamic performances in their control although they can suffer from noise and losses due to the higher harmonics spectrum [22–24]. Induction machines are a good choice in order to deal with these issues, as they are able to withstand higher temperature and are more robust toward harmonic current and ripples than synchronous motors.
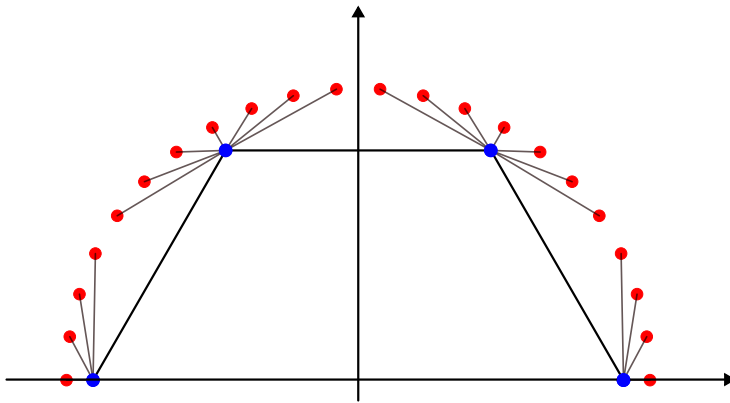
(a) Six-step representation on the $\alpha\beta$ plane
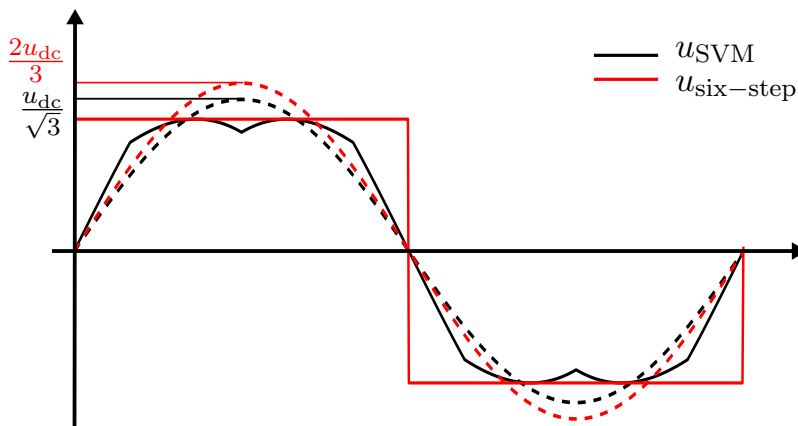
(b) Comparison between normal operation (black) and six-step mode (red): solid lines are the reference voltage, dotted lines are the fundamental components

Figure 2.3: Six-step mode in the $\alpha\beta$ plane and reference waveforms

2.2.2 Bolognani's overmodulation method

The solution proposed in [21] is one of the many techniques available to manage transition between normal operation and six-step mode. The main advantages concern the implementation simplicity and the linearity between the reference vector and the voltage output. The implementation of this technique is straightforward, a single algorithm is able to manage the transition from normal operation to six-step mode. The modulation index in (1.15) grows almost linearly in the overmodulation region, this feature assures a smooth transition toward six-step without the using any look-up table [22].

Bolognani's technique performs the following steps. Assuming a reference vector

in the polar form

$$\boldsymbol{u}_{\mathrm{ref}} = r\mathrm{e}^{\mathrm{j}\theta_1}$$

where r is the amplitude and θ_1 is the phase, the trajectory can be traced using standard SVM operation until it reaches the inscribed circumference. When its amplitude is greater than $u_{\mathrm{dc}}/\sqrt{3}$, a modified trajectory must be set.

Figure 2.4 shows the needed steps for managing the transition. In the first sector, assuming as initial condition $\theta_1 = 0$ and $u_{\mathrm{dc}}/\sqrt{3} \leqslant r \leqslant 2/3u_{\mathrm{dc}}$, the reference vector is modified in the following way:

- generation a voltage vector of amplitude r and phase θ_1 until its trajectory intersects the hexagon boundary in $\theta_1 = \alpha_{\mathrm{g}}$
- generation a fixed voltage vector of amplitude r and phase $\theta_1 = \alpha_{\mathrm{g}}$ for angles ranging from $\theta_1 = \alpha_{\mathrm{g}}$ to $\theta_1 = \pi/6$
- generation a fixed voltage vector of amplitude r and phase $\theta_1 = \pi/3 - \alpha_{\mathrm{g}}$ for angles ranging from $\theta_1 = \pi/6$ to $\theta_1 = \pi/3 - \alpha_{\mathrm{g}}$
- generation a vector that follows the reference, amplitude r and phase θ_1 from $\theta_1 = \pi/3 - \alpha_{\mathrm{g}}$ to $\theta_1 = \pi/3$

Summin up, the produced vector has constant amplitude
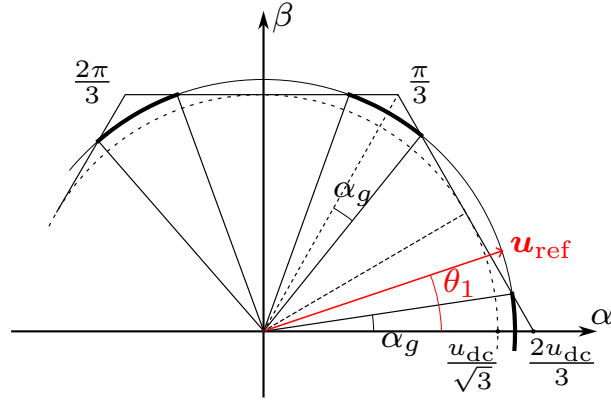
$$|\boldsymbol{u}| = r \tag{2.5}$$

and phase θ linked to the phase θ_1 of the reference vector by

$$\theta = \begin{cases} \theta_1 & 0 \leqslant \theta_1 \leqslant \alpha_{\mathrm{g}} \\ \alpha_{\mathrm{g}} & \alpha_{\mathrm{g}} \leqslant \theta_1 \leqslant \pi/6 \\ \pi/3 - \alpha_{\mathrm{g}} & \pi/6 \leqslant \theta_1 \leqslant \pi/6 - \alpha_{\mathrm{g}} \\ \theta_1 & \pi/3 - \alpha_{\mathrm{g}} \leqslant \theta_1 \leqslant \pi/3 \end{cases} \tag{2.6}$$
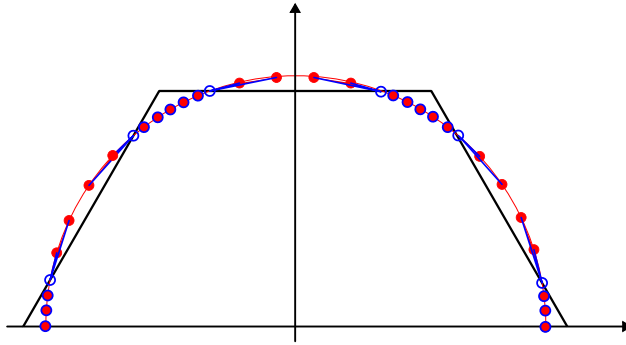
where α_{g} is found as

$$\alpha_{\mathrm{g}}(r) = \frac{\pi}{6} - \arccos\left(\frac{u_{\mathrm{dc}}}{r\sqrt{3}}\right) \tag{2.7}$$

The algorithm can be easily extended to the other sectors by symmetrically repeating what it is used in the first sector.

(a) Geometrical reconstruction of the reference vector [21]

(b) Starting reference vector (red) and vector realized after the overmodulation algorithm (blue) [24]

Figure 2.4: Continuous overmodulation strategy

2.3 Synchronized PWM

The mentioned PWM methods operate at constant carrier frequency while the fundamental frequency is varying. They have *asynchronous character* meaning that there is no relation between the system fundamental frequency and the sampling frequency.

The frequency modulation ratio is

$$m_\mathrm{f} = \frac{f_\mathrm{s}}{f_1} \tag{2.8}$$

where f_s is the sampling frequency and f_1 is the fundamental frequency of the reference. With asynchronous PWM, m_f is a decimal number that can vary during the operation. The Fourier spectrum is then wide and can contain frequencies lower than the lowest carrier sideband. These sub-harmonics in the output spectrum appear as low-frequency oscillation in currents and fluxes. The interaction between low order components and the fundamental component of flux or current generate low order torque harmonics that may stimulate resonances in the drive system [12,

25–28]. The low-frequency current can also create instability issues and increases losses in the system [23].

In order to improve the drive performance and the output waveforms, a synchronized PWM approach can be adopted. The switching frequency can be pre-selected in order for m_f to be integer.

2.4 Control methods for induction machines

Figure 2.5 shows the classification of control methods for induction machines. The first separation is between scalar and vector methods.

Scalar control was the first method to become popular. It refers to the steady-state model of the machine and adjusts magnitude and frequency of the applied stator voltage based on the desired speed reference. Thanks to its simplicity and low costs it is still widely used [29], [30]. Scalar control may suffer from stability problems, to reduce the unstable regions a compensator is often included.

Vector control schemes, on the other hand, are based on dynamic models. This means that there is an additional degree of freedom in the control system: in addition to magnitude and angular frequency, the instantaneous angular position of the stator voltage is controlled. As a result, the instantaneous position of current and flux linkages vectors can be independently controlled by the applied stator voltage vector. In this way, vector control methods allow to achieve a fast and accurate control of electromagnetic torque and flux magnitude. The two most popular schemes are the field-oriented control (FOC) and the direct torque control (DTC); sensorless vector control methods are also available [29], [31]. Conventional vector control adjusts both amplitude and phase of the inverter output meaning that six-step operation is not compatible with it since the phase angle is the only degree of freedom [24]. Drawbacks of vector control methods might include: sensitivity to parameters errors, need of a specific field-weakening algorithm, inability to exploit the full inverter voltage (a voltage reserve is needed for the current controller).

The control method proposed in [10] combines the simplicity of V/Hz control with some features of the sensorless field-oriented control. Furthermore it allows to avoid some of the drawbacks of both methods.
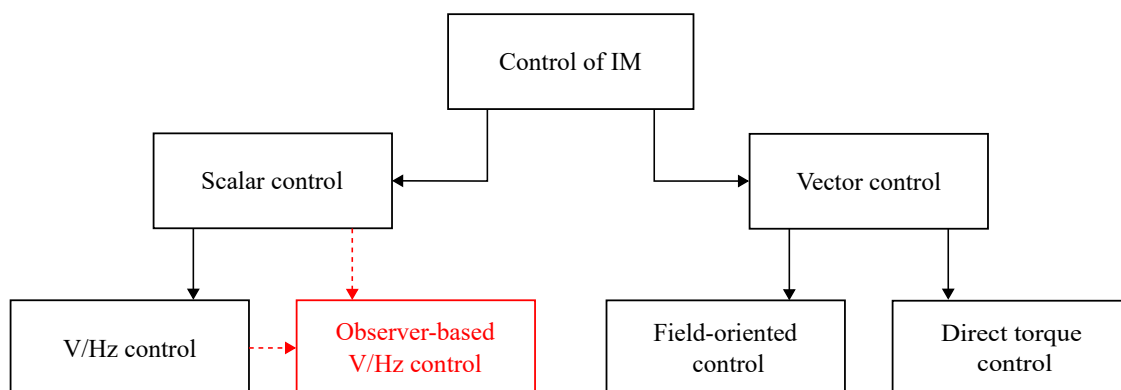

Figure 2.5: Classification of control methods for induction machines [29]

2.4.1 V/Hz control

V/Hz control is still a popular choice thanks to its simplicity and to the possibility of exploit the full inverter voltage [21], [32]. When working below the nominal speed, scalar control aims at keeping the stator flux magnitude close to its nominal value whatever speed and torque are produced. The flux amplitude is regulated adjusting the magnitude of the stator voltage as a function of the frequency. Applying Park transformation in (1.9) to the voltage equation in (1.25b) we obtain the voltage equation in a frame rotating at the stator frequency ω_s

$$\boldsymbol{u}_\mathrm{s} = R_\mathrm{s}\boldsymbol{i}_\mathrm{s} + \frac{\mathrm{d}\boldsymbol{\psi}_\mathrm{s}}{\mathrm{d}t} + \omega_\mathrm{s}\mathbf{J}\boldsymbol{\psi}_\mathrm{s} \tag{2.9}$$

By neglecting the stator resistance R_s and assuming a steady-state operation it is possible to cancel the first two terms of the previous equation. Assuming $\omega_\mathrm{s} = \omega_\mathrm{s,ref}$, where the slip frequency is neglected, the voltage reference can be computed as

$$\boldsymbol{u}_\mathrm{s,ref} = \omega_\mathrm{s,ref}\mathbf{J}\boldsymbol{\psi}_\mathrm{s,ref} \tag{2.10}$$

Since the ratio between the voltage amplitude and the stator frequency is constant, scalar method is often referred as *V/Hz control* [29].

One of the main problems related to this type of control concern stability; the interaction between the electrical and mechanical subsystems may lead to unstable regions at medium speed. Furthermore, the stator resistance voltage drop has to be compensated in order to maintain the desired flux level at low speed. Therefore a compensator is often used, it can include the compensation of both the stator resistance voltage drop and the steady-state speed error caused by the slip [1, 10]. Most of the times V/Hz control includes also a feedback from the stator current which helps to increase the robustness of the drive system [30].

Figure 2.6 shows the typical scheme of a compensated V/Hz control [10]. The voltage reference $\boldsymbol{u}_\mathrm{s,ref}$ is:

$$\boldsymbol{u}_\mathrm{s,ref} = \omega_\mathrm{s}\mathbf{J}\boldsymbol{\psi}_\mathrm{s,ref} + C(s)\boldsymbol{i}_\mathrm{s} \tag{2.11}$$

where $C(s)$ is the transfer function of the compensator. An example of a compensator can be:

$$C(s) = \underbrace{\frac{\alpha_1}{s + \alpha_1}R_\mathrm{s}\mathbf{I}}_{\text{RI compensation}} + \underbrace{\frac{s}{s + \alpha_2}k_\mathrm{u}L_\sigma\omega_\mathrm{s}\mathbf{J}}_{\text{Damping}} \tag{2.12}$$

where k_u is a positive gain and α_1, α_2 are low-pass and high-pass filter bandwidths respectively. In the same figure $F(s)$ represents the high-pass filter transfer function. $\hat{\tau}_\mathrm{m}'$ is the estimation of torque based on measured current and flux reference:

$$\hat{\tau}_\mathrm{m}' = \boldsymbol{i}_\mathrm{s}^\mathrm{T}\mathbf{J}\boldsymbol{\psi}_\mathrm{s,ref} \tag{2.13}$$

The stability and control performance depend on the compensator. Despite the literature about it [30], V/Hz control method cannot completely remove the unstable regions.
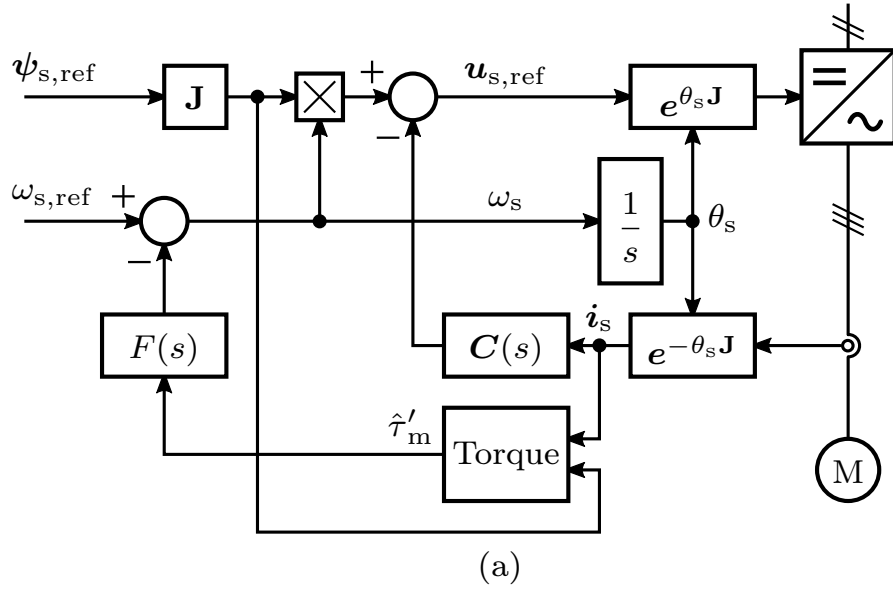
(a)

Figure 2.6: Conventional V/Hz control [10]

2.4.2 Observer-based V/Hz control

Figure 2.7 shows the block scheme of the method proposed in [10]. The two main additions are the state-feedback control law and the flux observer. As compared to conventional scalar control, this observer-based V/Hz control is stable in the whole feasible operating range while still ensuring a sensorless operation. Furthermore, it is possible to increase damping in the mechanical system by using an additional feedback from the electromagnetic torque estimate $\hat{\tau}_\mathrm{m}$ through the high-pass filter $F(s)$.

The voltage reference is computed as

$$\boldsymbol{u}_{\mathrm{s,ref}} = R_\mathrm{s}\boldsymbol{i}_\mathrm{s} + \omega_\mathrm{s}\mathbf{J}\boldsymbol{\psi}_{\mathrm{s,ref}} + \mathbf{K}(\boldsymbol{\psi}_{\mathrm{s,ref}} - \hat{\boldsymbol{\psi}}_\mathrm{s}) \tag{2.14}$$

where ω_s is the stator angular frequency, $\boldsymbol{\psi}_{\mathrm{s,ref}} = [\psi_{\mathrm{s,ref}}, 0]^\mathrm{T}$ is an external stator flux reference, $\hat{\boldsymbol{\psi}}_\mathrm{s}$ is the stator flux estimate provided by the observer and $\mathbf{K}$ is a 2x2 gain matrix. With $\mathbf{K} = \mathbf{0}$ the control law reduces to the one of conventional V/Hz with RI compensation.

The control law in (2.14) can be rewritten considering $\hat{\boldsymbol{\psi}}_\mathrm{s} = \hat{\boldsymbol{\psi}}_\mathrm{R} + L_\mathrm{s}\boldsymbol{i}_\mathrm{s}$:

$$\boldsymbol{u}_{\mathrm{s,ref}} = R_\mathrm{s}\boldsymbol{i}_\mathrm{s} + \omega_\mathrm{s}\mathbf{J}\boldsymbol{\psi}_{\mathrm{s,ref}} + L_\sigma\mathbf{K}(\boldsymbol{i}_{\mathrm{s,ref}} - \boldsymbol{i}_\mathrm{s}) \tag{2.15a}$$

$$\boldsymbol{i}_{\mathrm{s,ref}} = \frac{\boldsymbol{\psi}_{\mathrm{s,ref}} + \hat{\boldsymbol{\psi}}_\mathrm{R}}{L_\sigma} \tag{2.15b}$$

where $\boldsymbol{i}_{\mathrm{s,ref}}$ is an intermediate stator current reference that can be saturated if one wants to limit the stator current.

The internal stator frequency is found as

$$\omega_\mathrm{s} = \omega_{\mathrm{s,ref}} - k_\omega(\hat{\tau}_\mathrm{m} - \hat{\tau}_{\mathrm{mf}}) \tag{2.16}$$

25

where $\omega_{\mathrm{s,ref}}$ is an external rate-limited stator frequency reference, $\hat{\tau}_{\mathrm{m}}$ is the torque estimate, k_ω is a positive gain that increases the damping. $\hat{\tau}_{\mathrm{mf}}$ is a low-pass filtered torque estimate

$$\frac{\mathrm{d}\hat{\tau}_{\mathrm{mf}}}{\mathrm{d}t} = \alpha_{\mathrm{f}}(\hat{\tau}_{\mathrm{m}} - \hat{\tau}_{\mathrm{mf}}) \tag{2.17}$$

where α_{f} is the bandwidth of the filter. The stator frequency becomes

$$\omega_{\mathrm{s}} = \omega_{\mathrm{s,ref}} - \frac{k_\omega s}{s + \alpha_{\mathrm{f}}}\hat{\tau}_{\mathrm{m}} = \omega_{\mathrm{s,ref}} - F(s)\hat{\tau}_{\mathrm{m}} \tag{2.18}$$

The stator flux linkage is estimated by means of a reduced-order flux observer. Starting from equation (1.28b), it can be formulated as

$$\frac{\mathrm{d}\hat{\boldsymbol{\psi}}_{\mathrm{R}}}{\mathrm{d}t} = \boldsymbol{u}_{\mathrm{s,ref}} - (R_{\mathrm{s}}\mathbf{I} + \omega_{\mathrm{s}}L_\sigma\mathbf{J})\boldsymbol{i}_{\mathrm{s}} - L_\sigma\frac{\mathrm{d}\boldsymbol{i}_{\mathrm{s}}}{\mathrm{d}t} - \omega_{\mathrm{s}}\mathbf{J}\hat{\boldsymbol{\psi}}_{\mathrm{R}} + \mathbf{K}_{\mathrm{o}}\boldsymbol{e} \tag{2.19}$$

where $\mathbf{K}_{\mathrm{o}}$ is a 2x2 observer gain matrix. The output equations are

$$\hat{\boldsymbol{\psi}}_{\mathrm{s}} = \hat{\boldsymbol{\psi}}_{\mathrm{R}} + L_\sigma\boldsymbol{i}_{\mathrm{s}} \tag{2.20a}$$

$$\hat{\tau}_{\mathrm{m}} = \boldsymbol{i}_{\mathrm{s}}^{\mathrm{T}}\mathbf{J}\hat{\boldsymbol{\psi}}_{\mathrm{R}} \tag{2.20b}$$

The correction vector obtained from (1.28a) is

$$\boldsymbol{e} = L_\sigma\frac{\mathrm{d}\boldsymbol{i}_{\mathrm{s}}}{\mathrm{d}t} + (R_\sigma\mathbf{I} + \omega_{\mathrm{s}}L_\sigma\mathbf{J})\boldsymbol{i}_{\mathrm{s}} - (\alpha\mathbf{I} - \hat{\omega}_{\mathrm{m}}\mathbf{J})\hat{\boldsymbol{\psi}}_{\mathrm{R}} - \boldsymbol{u}_{\mathrm{s,ref}} \tag{2.21}$$

where $\hat{\omega}_{\mathrm{m}}$ is the speed estimate that can be computed by integrating the component of $\boldsymbol{e}$ orthogonal to the rotor flux estimate

$$\frac{\mathrm{d}\hat{\omega}_{\mathrm{m}}}{\mathrm{d}t} = \alpha_{\mathrm{o}}\frac{\hat{\boldsymbol{\psi}}_{\mathrm{R}}^{\mathrm{T}}\mathbf{J}\boldsymbol{e}}{||\hat{\boldsymbol{\psi}}_{\mathrm{R}}||^2} \tag{2.22}$$

where α_{o} is the speed-estimation bandwidth.

(b)

Figure 2.7: Observer-based V/Hz control in [10]

3.   Simulations and results

In this chapter the described models are used to analyze the compatibility between the control method and the operation in six-step mode.

In the beginning, benefits of the observer-based V/Hz control are shown. Then all the simulation concerning the topic of thesis are carried out. A first simulation is made with the conventional open-loop V/Hz control in order to test the overmodulation algorithm. Then the overmodulation algorithm is applied to the observer-based V/Hz control to test the compatibility. Synchronized PWM is then added in order to reduce the ripple in the torque.

Simulations are done using *Motulator*, an open source Python platform [17].

3.1   System parameters

The chosen motor is a 2.2 kW induction motor described with the *Inverse-Γ model* with the parameters shown in table 3.1.

Parameters	Symbol	Value
Nominal power	P_n	2.2 kW
Nominal torque	τ_n	14.6 N m
Nominal voltage	U_n	400 V
Nominal current	I_n	5 A
Nominal speed	ω_n	1436 rpm
Nominal frequency	f_n	50 Hz
Number of pole pairs	p	2
Stator resistance	R_s	3.7 Ω
Rotor resistance	R'_R	2.1 Ω
Leakage inductance	L'_σ	21 mH
Magnetizing inductance	L'_M	224 mH

The inverter dc link is set as $u_\mathrm{dc} = 540\,\mathrm{V}$.

Assuming the coupling between motor and load as rigid the only parameter to be defined is the total moment of inertia set as $J_\mathrm{m} = 0.016\,\mathrm{kgm^2}$.

A quadratic load torque profile is used in order to simulate the high speed applications mentioned in the introduction. The external load torque in (1.30) is set to 0 and the parameter k in (1.32) is set to $k = 0.2$.

3.2 Benefit of the observer-based V/Hz control

Figure 3.1 shows the benefit of adding the observer to the V/Hz control. The same speed and torque profile are simulated respectively with an open-loop V/Hz control (figure 3.1a), a compensated V/Hz control (figure 3.1b) and the observer-base V/Hz control (figure 3.1c). With the first two control methods, the system is either unstable or poorly damped. On the other hand, with the third method, the system is stable and well damped. The dynamic of the control is fast and the speed profile is followed precisely.

(a) (b) (c)
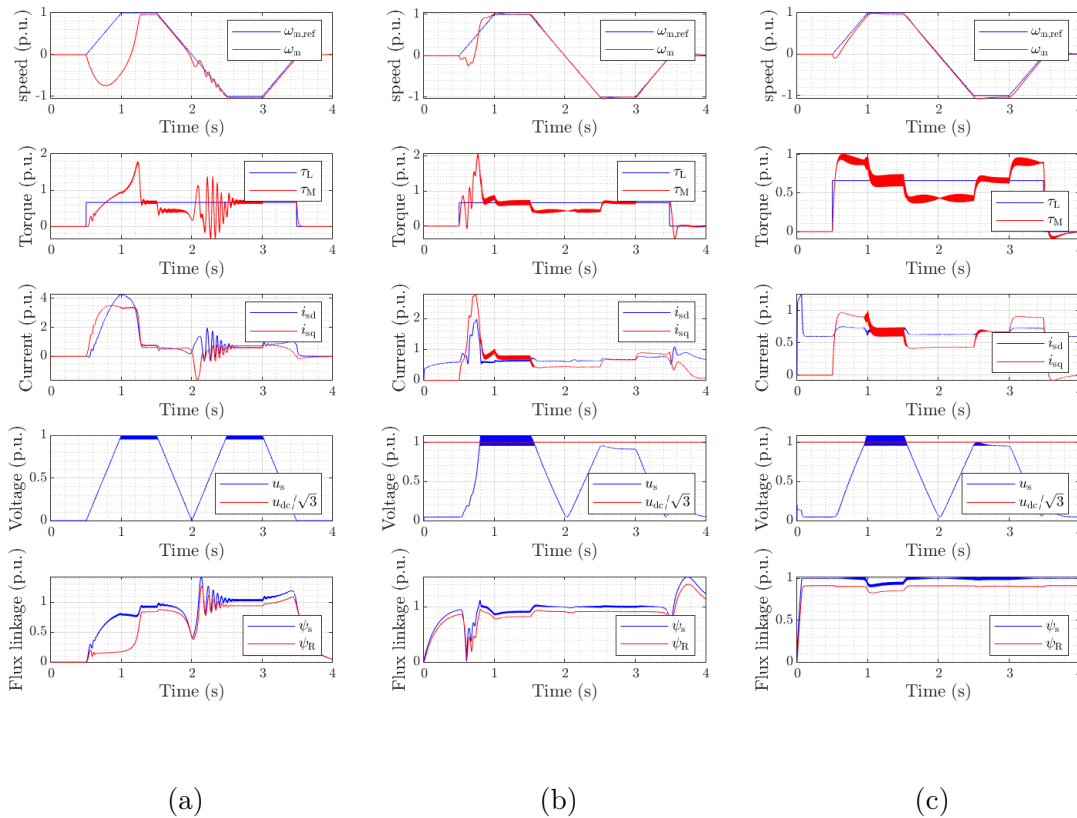
Figure 3.1: Comparison between different scalar controls: (a) open-loop V/Hz; (b) compensated V/Hz control; (c) observer-based V/Hz control [10]

3.3 Simulations with conventional V/Hz control

The first simulation tests the overmodulation algorithm on a conventional open-loop V/Hz control (figure 2.6). The speed reference is set as ramp from $\omega_{\mathrm{m,ref}} = 0$ to $2\omega_{\mathrm{m,nom}}$.

Figure 3.2 shows the results of the simulations. The system is stable but from the beginning of the overmodulation region to the six-step mode currents and torque present high ripples. This is caused by the presence of subharmonics in the output spectrum.

Figure 3.2: Results with conventional scalar control
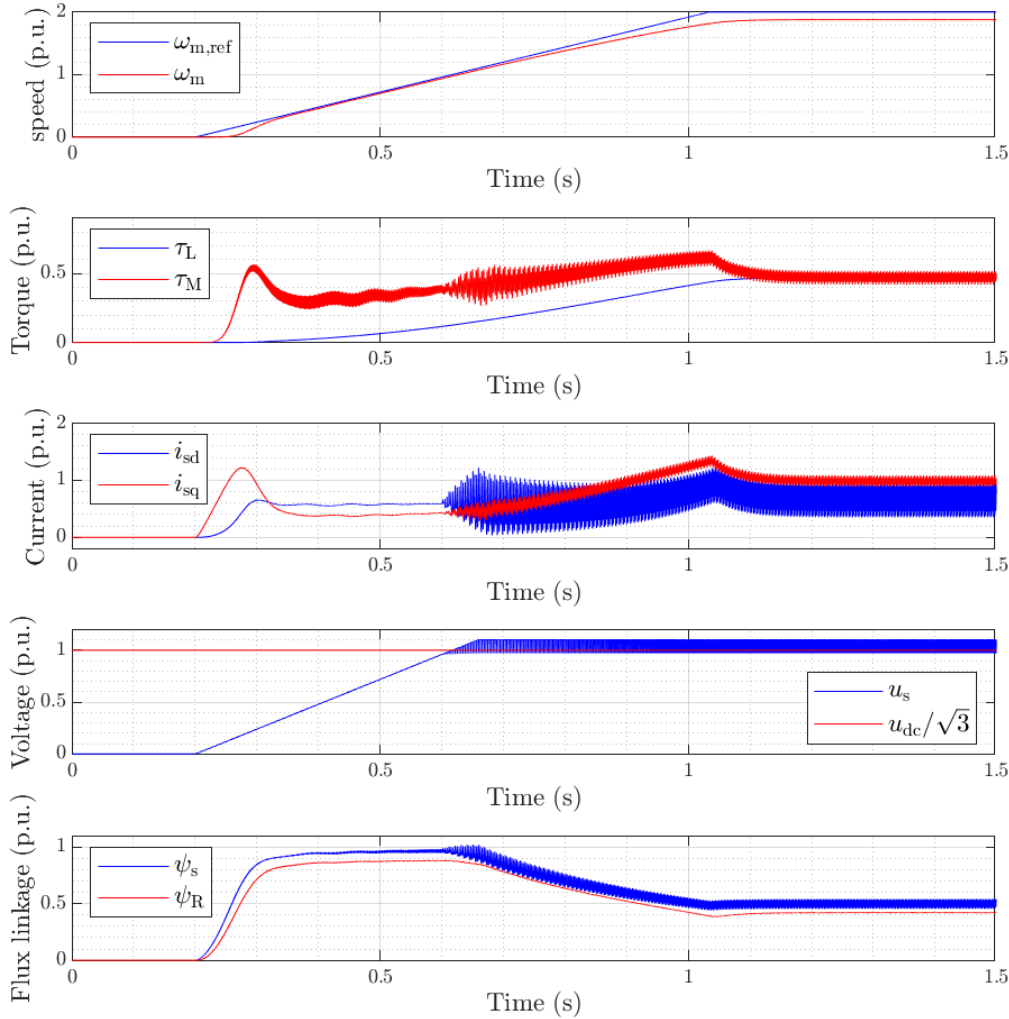
Figure 3.3: Results with conventional scalar control and synchronized PWM

On the other hand, the ripple in the voltage is fictitious, $\boldsymbol{u}_\mathrm{s}$ is a signal used inside the controller to compute references. It is based on the reference voltage vector produced by the control system after the computation of duty cycles. Each value of $\boldsymbol{u}_\mathrm{s}$ is made of the average between two consecutive samples, this means that when the output vector changes from one state to another the average vector has the same amplitude but the average of the phases of the two output state. During six-step mode, this results in a ripple with a frequency of one sixth the switching frequency. In reality, the magnitude of the stator voltage vector is constant and equal to $|\boldsymbol{u}_\mathrm{s}| = 2u_\mathrm{dc}/3$.

In order to get rid of subharmonics and improve the output waveforms, a synchronized approach is adopted for the next simulations. When the voltage reference

vector lays in the overmodulation region, the sampling frequency f_s is selected as

$$f_s = \frac{N_s \omega_s}{2\pi} = \frac{100 \omega_s}{2\pi} \tag{3.1}$$

so that it is a integer multiple of the fundamental frequency of the system. The number N_s is the number of samplings in one period. Appendix B shows the digital implementation of the sampling synchronization.

Results adopting this approach are shown in figure 3.3. Ripple in currents and torque is significantly reduced but still high. When zooming on the voltage reference, it is possible to recognize to waveform proper of Bolognani's overmodulation method (equations (2.5), (2.6)), as shown in figure 3.4. The reference voltage smoothly transitions from a sinusoidal wave (normal condition) to the six-step reference. Appendix A shows the digital implementation of the algorithm.
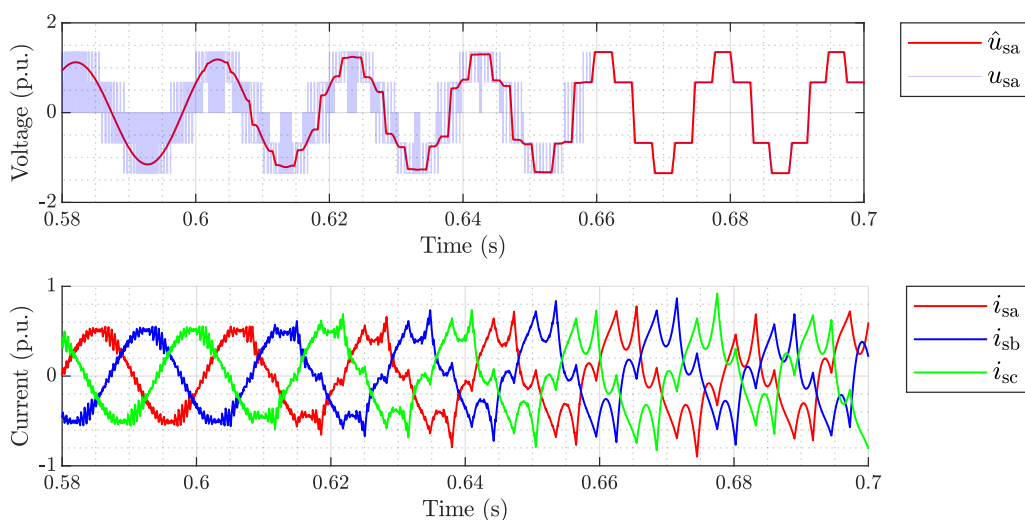
Figure 3.4: Reference and output voltage and current in the transition from normal operation to six-step

3.4   Simulations with observer-based V/Hz control

The same simulations were done with the observer-based V/Hz control. Results without and with synchronized PWM are presented respectively in figures 3.5 and 3.6. The observer-based V/Hz control is able to work in six-step mode, the closed-loop control does not influence the operation in six-step.
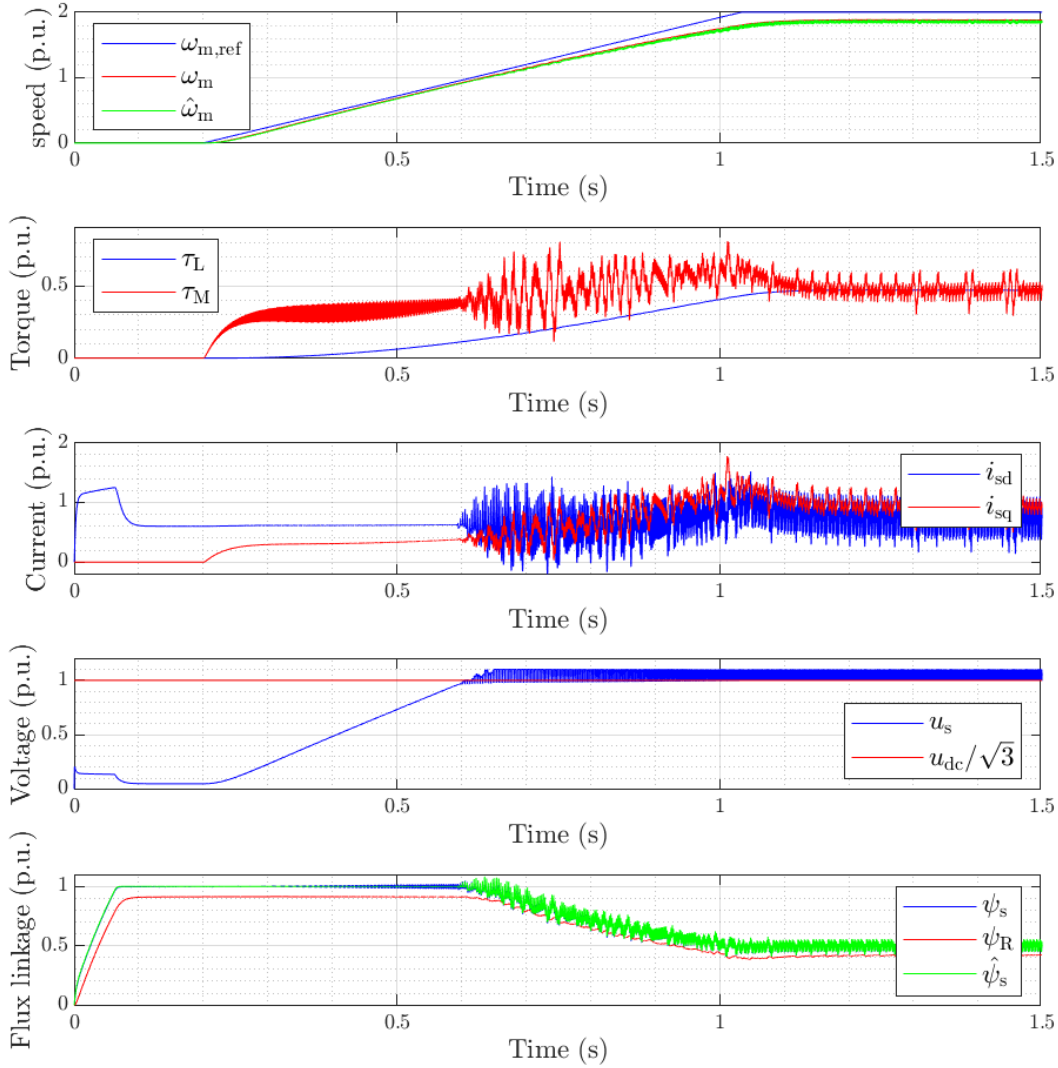
Figure 3.5: Results with observer-based V/Hz control
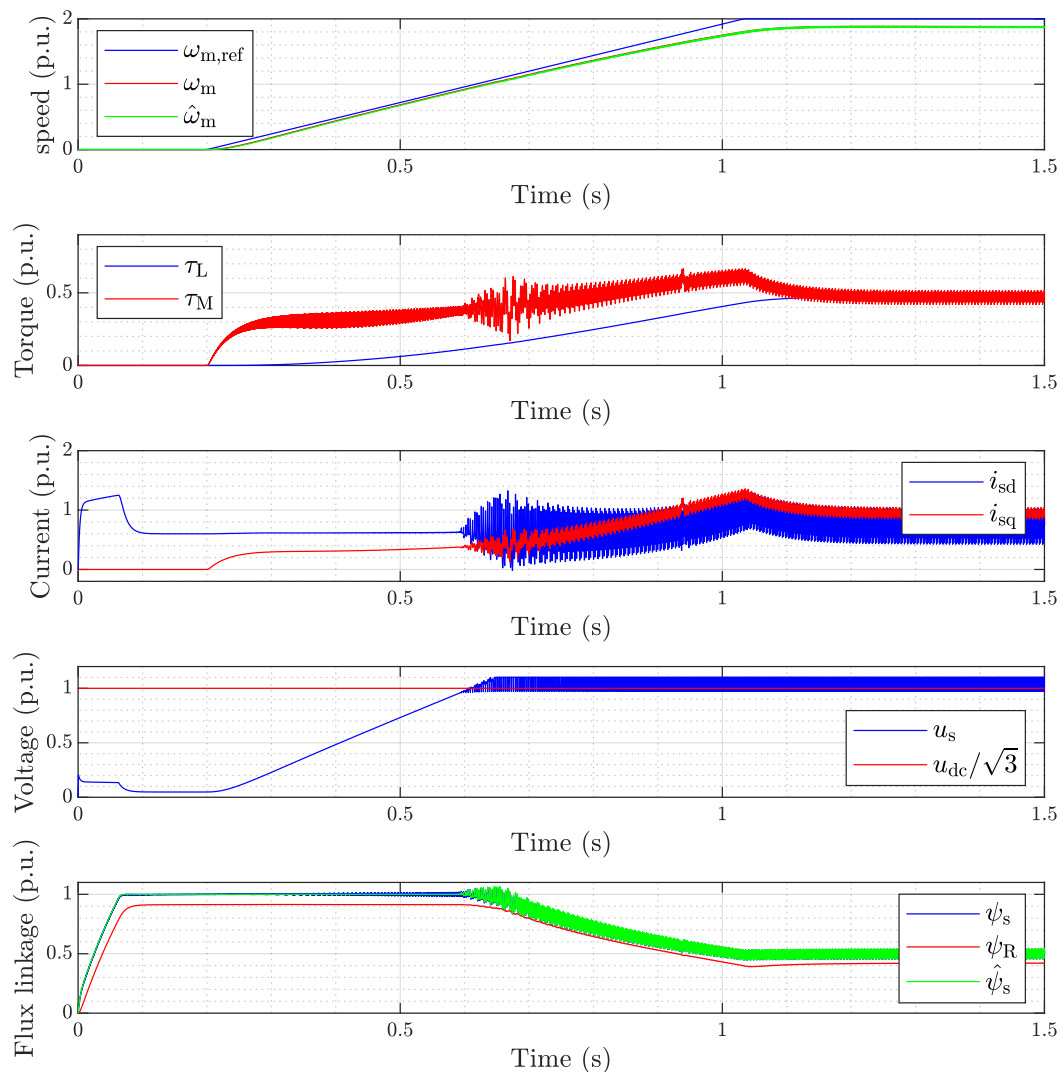
Figure 3.6: Results with observer-based V/Hz control and synchronized PWM

Synchronization is able to improve significantly the output spectrum reducing torque and current ripple.

Comparing conventional V/Hz (figure 3.3) with the observer-based V/Hz it is possible to notice a slight improvement in the response to the speed reference in the low speed region. performance does not improve significantly with this reference.

Figures 3.7 and 3.8 show the same two control methods with a new possible sequence where the speed is varied from $\omega_{\mathrm{m,ref}} = 0$ to $2 \cdot \omega_{\mathrm{m,nom}}$, then to $2 \cdot \omega_{\mathrm{m,nom}}$ and back to $1.5 \cdot \omega_{\mathrm{m,nom}}$. In this case it is possible to notice how the damping in torque and current profiles increases when using the observer-based V/Hz control.
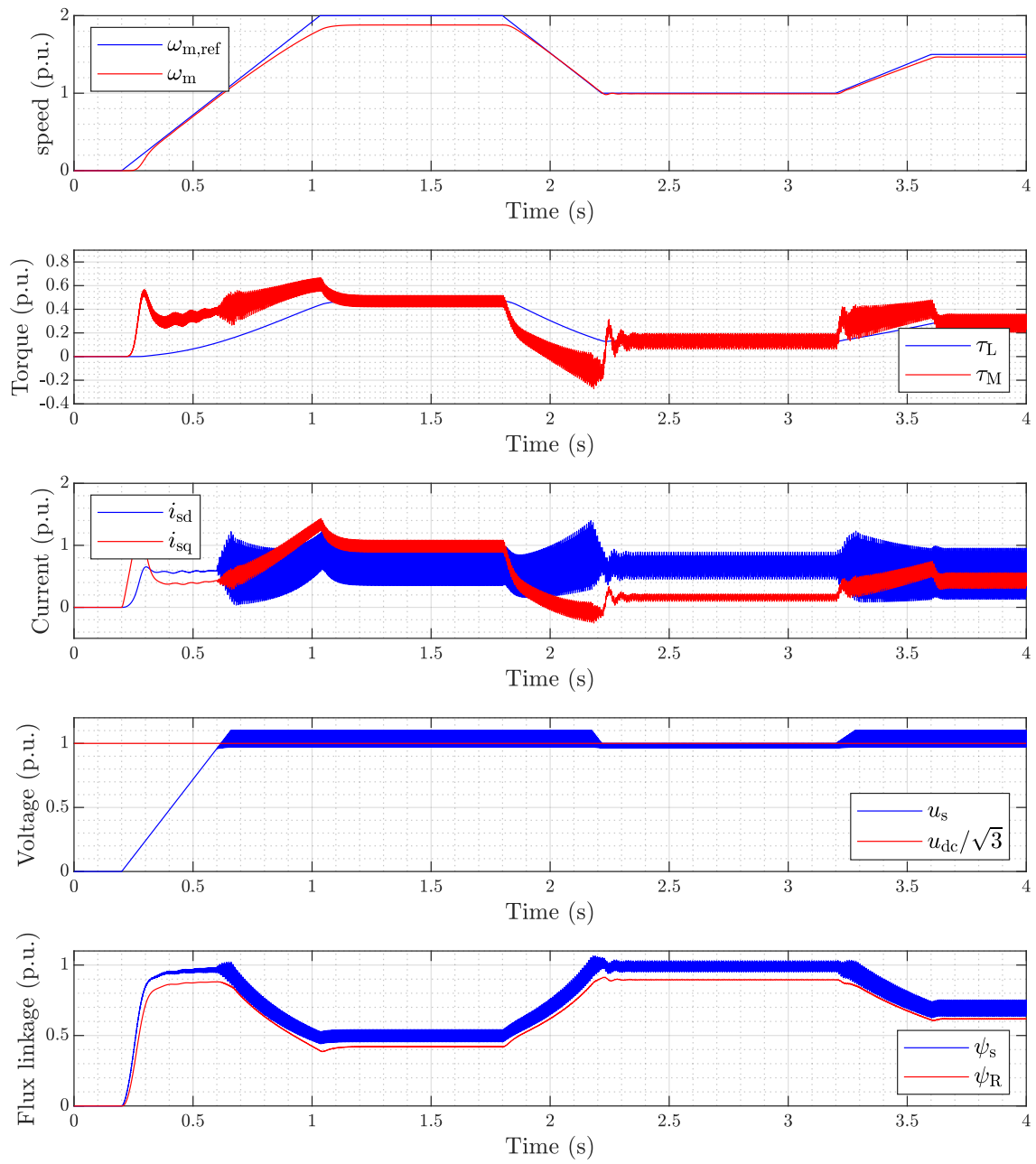
Figure 3.7: Results with V/Hz control and a new sequence

Figure 3.8: Results with observer-based V/Hz control and a new sequence

3.5 Comparison between six-step mode and traditional overmodulation algorithm

In order to further analyze the six-step operating mode, it is useful to compare this condition with a traditional overmodulation operation implementing the MPE method shown in figure 2.2. With a reference vector that lays outside the hexagon, the control algorithm cuts its amplitude to the hexagon boundary mantaining the original phase. Results are shown in figure 3.9.
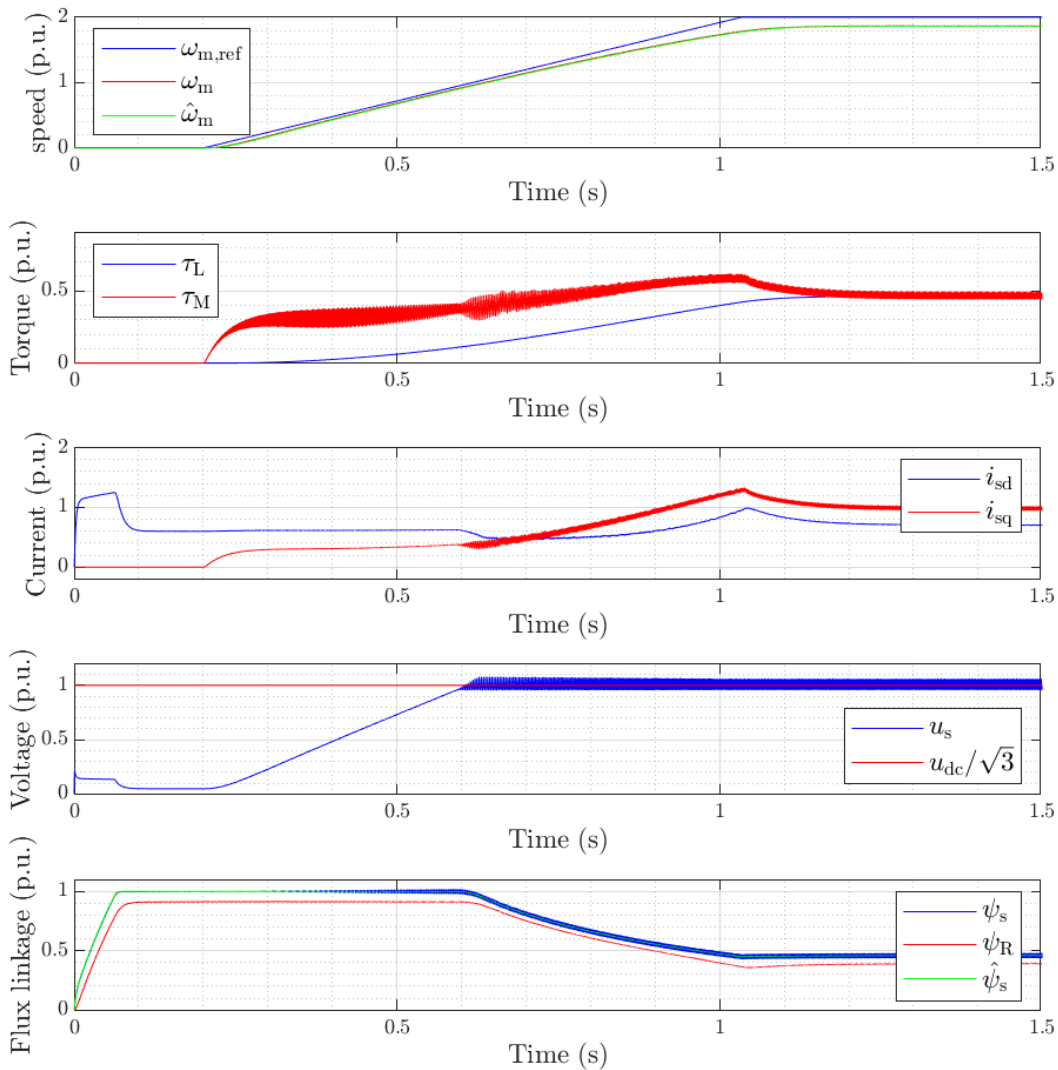
Figure 3.9: Results with observer-based V/Hz control working with MPE overmodulation algorithm

When comparing results in figure 3.6 and 3.9 it is possible to confirm that the average voltage when working in six-step mode is higher compared to MPE operation. Having higher voltage means that flux linkages and torque are also higher. In this way the average current is lower and the speed reached in steady state greater. This operating condition allows to have higher torque in the field-weakening region. As a drawback the ripple in the torque and in currents is higher but when dealing with high-speed applications ripple is always present.

4.   Conclusion

This thesis analyzed the overmodulation operation of an induction machine equipped with an observer-based V/Hz control. The goal was to study the behaviour of the control algorithm when working in six-step mode, condition that allows to maximize the voltage.

The overmodulation operating condition is reached when the speed exceeds its nominal value, in this condition the machine is working in the field-weakening region. In order to maximize the speed, the maximum voltage is needed. The second chapter explained in detail the possible overmodulation algorithms that can be used and, among them, six-step mode is the one that allows to exploit the full inverter voltage. Six-step mode brings out some drawbacks: the harmonic spectrum of the output is greater, harmonic currents flow in the system increasing losses, noise and vibrations. An induction machine is chosen to face these issues, thanks to its robustness against harmonics. Furthermore, with the increase in speed, subharmonics in current and torque can appear causing additional ripples. To avoid this issue, a synchronized PWM approach was adopted. By making the switching frequency an integer multiple of the stator voltage it is possible to cancel these subharmonics and improve the output waveforms.

Simulations bring the desired results: the observer-based V/Hz control is able to work in six-step mode and, when adopting the synchronized approach, torque and current ripples are minimized. Compared to the standard overmodulation operating condition, six-step is able to provide higher torque and then to maximize the speed. On the other hand, with six-step the harmonic spectrum is greater and harmonic losses higher.

The convenience of this configuration depends on the type of application. When dealing with high-speed applications, having higher voltage and lower current is beneficial in order to lower copper losses. On the other hand, higher torque ripple means higher noise in the system.

Experimental tests could be carried out to verify the simulation results.

Bibliography

[1] Zhe Zhang and Ali M. Bazzi. Robust sensorless scalar control of induction motor drives with torque capability enhancement at low speeds. In *2019 IEEE International Electric Machines & Drives Conference (IEMDC)*, pages 1706–1710, 2019.

[2] A. Munoz-Garcia, T.A. Lipo, and D.W. Novotny. A new induction motor V/f control method capable of high-performance regulation at low speeds. *IEEE Transactions on Industry Applications*, 34(4):813–821, 1998.

[3] Gwon-Jae Jo and Jong-Woo Choi. Rotor field-oriented V/ f drive system implementation with oscillation suppression compensator in induction motors. *IEEE Journal of Emerging and Selected Topics in Power Electronics*, 9(3):2745–2758, 2021.

[4] Juha Pyrhonen, Janne Nerg, Panu Kurronen, and Uwe Lauber. High-speed high-output solid-rotor induction-motor technology for gas compression. *IEEE Transactions on Industrial Electronics*, 57(1):272–280, 2010.

[5] W.L. Soong, G.B. Kliman, R.N. Johnson, R.A. White, and J.E. Miller. Novel high-speed induction motor for a commercial centrifugal compressor. *IEEE Transactions on Industry Applications*, 36(3):706–713, 2000.

[6] Sumit Singhal. Electric drive compressor systems: High-speed turbo compressors used in the oil and gas industry. *IEEE Industry Applications Magazine*, 20(6):52–63, 2014.

[7] T. Halkosaari. Optimal U/f-control of high speed permanent magnet motors. In *2006 IEEE International Symposium on Industrial Electronics*, volume 3, pages 2303–2308, 2006.

[8] David Gerada, Abdeslam Mebarki, Neil L. Brown, Chris Gerada, Andrea Cavagnino, and Aldo Boglietti. High-speed electrical machines: Technologies, trends, and developments. *IEEE Transactions on Industrial Electronics*, 61(6):2946–2959, 2014.

[9] P. Adam, M. Barton, K. Lake, and M. Schulz. *Hydrogen compression – An integral part of the H_2 value chain*. Siemens Energy 2021 Siemens Gas and Power GmbH & Co. KG Germany Siemens Energy Inc. United States, 2021.

[10] Lauri Tiitinen, Marko Hinkkanen, and Lennart Harnefors. Stable and passive observer-based V/Hz control for induction motors. In *2022 IEEE Energy Conversion Congress and Exposition (ECCE)*, pages 1–8, 2022.

[11] Simone Buso, Paolo Mattavelli. *Digital Control in Power Electronics*. Morgan & Claypol Publishers, San Rafael, California, USA, 2015.

[12] Bimal K. Bose. *Power Electronics and Variable Frequency Drives*. IEEE Press, 345 East 47th Street, New York, USA, 1997.

[13] Ned Mohan, Tore M. Undeland, William P. Robbins. *Power Electronics: Converters, Applications and Design*. John Wiley & Sons, Inc., Hoboken, New Jersey, USA, 1995.

[14] J. Holtz, W. Lotzkat, and A.M. Khambadkone. On continuous control of pwm inverters in the overmodulation range including the six-step mode. *IEEE Transactions on Power Electronics*, 8(4):546–553, 1993.

[15] H.W. van der Broeck, H.-C. Skudelny, and G.V. Stanke. Analysis and realization of a pulsewidth modulator based on voltage space vectors. *IEEE Transactions on Industry Applications*, 24(1):142–150, 1988.

[16] G.R. Slemon. Modelling of induction machines for electric drives. *IEEE Transactions on Industry Applications*, 25(6):1126–1131, 1989.

[17] Aalto Electric Drives. Motulator source code. `https://github.com/Aalto-Electric-Drives/motulator`. Accessed 5 September 2022.

[18] A.M. Hava, R.J. Kerkman, and T.A. Lipo. Simple analytical and graphical methods for carrier-based pwm-vsi drives. *IEEE Transactions on Power Electronics*, 14(1):49–61, 1999.

[19] Jul-Ki Seok and Seung-Ki Sul. A new overmodulation strategy for induction motor drive using space vector pwm. *Proceedings of 1995 IEEE Applied Power Electronics Conference and Exposition - APEC'95*, 1:211–216 vol.1, 1995.

[20] Jul-Ki Seok, Jhoon-Sheok Kim, Jong-Woo Choi, and Seung-Ki Sul. Overmodulation strategy for high performance torque control. *PESC Record. 27th Annual IEEE Power Electronics Specialists Conference*, 2:1549–1554 vol.2, 1996.

[21] S. Bolognani and M. Zigliotto. Novel digital continuous control of svm inverters in the overmodulation range. *IEEE Transactions on Industry Applications*, 33(2):525–530, 1997.

[22] Heekwang Lee, Seungmin Hong, Jongwon Choi, Kwanghee Nam, and Jaehong Kim. Sector-based analytic overmodulation method. *IEEE Transactions on Industrial Electronics*, 66(10):7624–7632, 2019.

[23] Jaeyong Park, Sungho Jung, and Jung-Ik Ha. Variable time step control for six-step operation in surface-mounted permanent magnet machine drives. *IEEE Transactions on Power Electronics*, 33(2):1501–1513, 2018.

[24] Yong-Cheol Kwon, Sungmin Kim, and Seung-Ki Sul. Six-step operation of pmsm with instantaneous current control. *IEEE Transactions on Industry Applications*, 50(4):2614–2625, 2014.

[25] V. Oleschuk and F. Blaabjerg. Algebraic and trigonometric algorithms of synchronized pwm for variable speed drives. In *2002 International Conference on Power Electronics, Machines and Drives (Conf. Publ. No. 487)*, pages 86–91, 2002.

[26] Avanish Tripathi and G. Narayanan. Analytical evaluation and reduction of torque harmonics in induction motor drives operated at low pulse numbers. *IEEE Transactions on Industrial Electronics*, 66(2):967–976, 2019.

[27] Avanish Tripathi and G. Narayanan. Evaluation and minimization of low-order harmonic torque in low-switching-frequency inverter-fed induction motor drives. *IEEE Transactions on Industry Applications*, 52(2):1477–1488, 2016.

[28] Haitao Yang, Yongchang Zhang, Guofeng Yuan, Paul D. Walker, and Nong Zhang. Hybrid synchronized pwm schemes for closed-loop current control of high-power motor drives. *IEEE Transactions on Industrial Electronics*, 64(9):6920–6929, 2017.

[29] Tobias Geyer. *Model Predictive Control of High Power Converters and Industrial Drives*. John Wiley & Sons, Inc., Hoboken, New Jersey, USA, 2016.

[30] Marko Hinkkanen, Lauri Tiitinen, Eemeli Mölsä, and Lennart Harnefors. On the stability of volts-per-hertz control for induction motors. *IEEE Journal of Emerging and Selected Topics in Power Electronics*, 10(2):1609–1618, 2022.

[31] Ion Boldea, Syed A. Nasar. *Electric Drives*. CRC Press, Boca Raton, Florida, USA, 1999.

[32] A.M. Hava, Seung-Ki Sul, R.J. Kerkman, and T.A. Lipo. Dynamic overmodulation characteristics of triangle intersection pwm methods. *IEEE Transactions on Industry Applications*, 35(4):896–907, 1999.

List of Figures

Appendix 1: Motulator

Simulations were done on Python, the platform used is open-source and available on GitHub [17]. *Motulator* is constructed as a sampled-data system that consists of a continuous-time system interfaced with a discrete-time system.

Figure 1 shows the generic structure of a sampled-data system: the continuous-time system (in red) is the model of a physical motor drive system that typically includes motor, mechanics and power converter. Inside *Motulator* the physical system quantities are indicated by the prefix `mdl`.

The discrete-time controller (in blue) contains control algorithms such as the current control and speed control. Inside *Motulator* the controller quantities are indicated by the prefix `ctrl`.

Digital control systems usually have a computational delay of one sampling period. This delay is modeled inside the class `motulator.simulation.Delay`. The carrier comparison is implemented in the class `motulator.simulation.CarrierCmp`
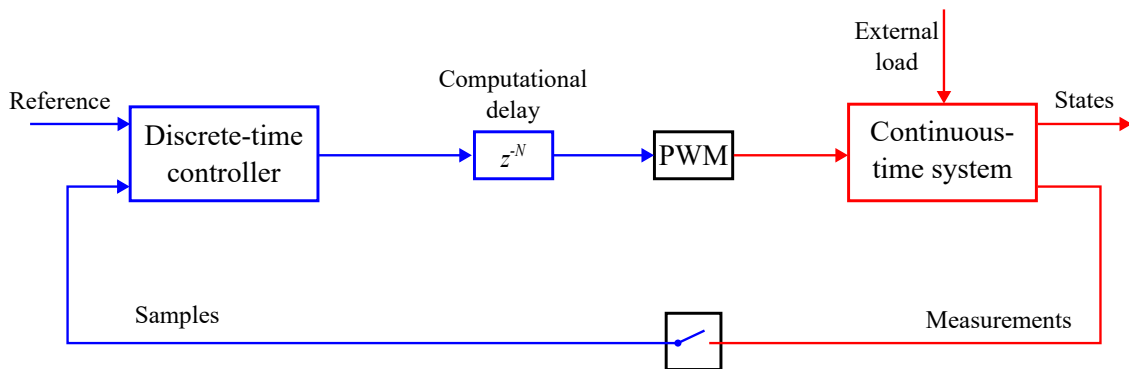

Figure 1: Block diagram of a sampled-data system. Discrete signals and systems are shown in blue, and continuous signals and systems are shown in red

A simulation file is contructed in the following way:

```python
# Import the packages.
import numpy as np
import motulator as mt
import scipy.io


# Configure the system model.


# Configure the induction motor using its inverse-gamma
# parameters
motor = mt.InductionMotorInvGamma(R_s=3.7, R_R=2.1,
        L_sgm=.021, L_M=.224, p=2)
mech = mt.Mechanics(J=.016) #Mechanics model
conv = mt.Inverter(u_dc=540) #Inverter model
```

```
mdl = mt.InductionMotorDrive(motor, mech, conv) #System model

# %%
# Configure the control system.
ctrl = mt.InductionMotorVHzObsCtrl(
    mt.InductionMotorObsVHzCtrlPars(six_step=False,
                                    slip_compensation=False))

# %%
# Set the speed reference.
# Speed reference
times = np.array([0, .125, .25, .375, .5, .625, .75, .875, 1])*4
values = np.array([0, 0, 1, 1, 0, -1, -1, 0, 0])*base.w
ctrl.w_m_ref = mt.Sequence(times, values)

# Set the load torque reference
times = np.array([0, .125, .125, .875, .875, 1])*4
values = np.array([0, 0, 1, 1, 0, 0])*base.tau_nom
mdl.mech.tau_L_t = mt.Sequence(times, values)

# %%
# Create the simulation object and simulate it.

sim = mt.Simulation(mdl, ctrl, pwm=True, delay=1)
sim.simulate(t_stop=4)

# %%
# Plot results in per-unit values. By omitting the argument
# base' you can plot the results in SI units.

mt.plot(sim, base=base)
scipy.io.savemat('observer_MPE_control.mat',ctrl.data)
scipy.io.savemat('observer_MPE_model.mat',mdl.data)
```

Appendix 2: Code snippets

A   Overmodulation algorithm

In order to build the simulations, Bolognani's overmodulation algorithm and the six-step mode had been implemented and added on the pre-existing module.

The implementation in Python language is shown below where `complex2abc` is the inverse of Clarke transformation in (1.4). When setting the control method in the main script, it is possible to enable the six-step mode by adding the parameter `six_step=True`.

When the six-step mode is enabled, the voltage reference vector is manipulated before computing the duty ratios

```python
def duty_ratios(u_s_ref, u_dc):
    # Modify angle in the overmodulation region
    if self.six_step:
        u_s_ref = self.six_step_overmodulation(u_s_ref,
                        u_dc)

    # Duty ratios
    d_abc_ref = self.duty_ratios(u_s_ref, u_dc)
```

When entering the `six_step_overmodulation` function, the voltage reference vector is modified as explained in section 2.2.2:

```python
def six_step_overmodulation(u_s_ref, u_dc):

    # Limited magnitude
    r = np.min([np.abs(u_s_ref), 2/3*u_dc])

    if np.sqrt(3)*r > u_dc:
        # Angle and sector of the reference vector
        theta = np.angle(u_s_ref)
        sector = np.floor(3*theta/np.pi)

        # Angle reduced to the first sector (at which
        # sector == 0)
        theta0 = theta - sector*np.pi/3

        # Intersection angle
        alpha_g = np.pi/6 - np.arccos(u_dc/(np.sqrt(3)*r))

        # Modify the angle
```

```python
        if alpha_g <= theta0 <= np.pi/6:
            theta0 = alpha_g
        elif np.pi/6 <= theta0 <= np.pi/3 - alpha_g:
            theta0 = np.pi/3 - alpha_g

        # Modified reference voltage
        u_s_ref_mod = r*np.exp(1j*(theta0 + sector*np.pi/3))
    else:
        u_s_ref_mod = u_s_ref

    return u_s_ref_mod
```

The modified reference voltage is then used to compute duty ratios.

B   Synchronization

The synchronization in (3.1) is implemented in the following way.

```python
# When the reference exceeds the inside circle, a synchro-
# nized approach is adopted
if np.abs(u_s_ref) > u_dc/np.sqrt(3):
        self.T_s = 2*np.pi/(100*np.abs(w_s))
    else:
        self.T_s = 200e-6
```